TRIBHUVAN UNIVERSITY

INSTITUTE OF ENGINEERING

PULCHOWK CAMPUS

THESIS NO. PUL080MSGtE012

3D FEM Based Service Life Evaluation of Geogrid Reinforced Flexible Pavements Under Heavy Vehicle Loading in Combined Curvature Gradient Sections

by

Prashanna Shrestha

A THESIS

SUBMITTED TO THE DEPARTMENT OF CIVIL ENGINEERING IN PARTIAL FULFILLMENT OF THE REQUIREMENTS FOR THE DEGREE OF MASTER IN GEOTECHNICAL ENGINEERING

DEPARTMENT OF CIVIL ENGINEERING

LALITPUR, NEPAL

APRIL, 2026

COPYRIGHT

Asst. Prof. Dr. Ram Krishna Regmi

Head

Department of Civil Engineering

Pulchowk Campus, Institute of Engineering

Pulchowk, Lalitpur

Nepal

TRIBHUVAN UNIVERSITY

INSTITUTE OF ENGINEERING

PULCHOWK CAMPUS

DEPARTMENT OF CIVIL ENGINEERING

The thesis titled "3D FEM Based Service Life Evaluation of Geogrid Reinforced Flexible Pavements under Heavy Vehicle Loading in Combined Curvature Gradient Sections" prepared and submitted by Prashanna Shrestha in partial fulfilment of the requirements for the degree of Master of Science in Geotechnical Engineering has been examined by us and is accepted for the award of M. Sc. in Geotechnical Engineering by Tribhuvan University.

The undersigned certify that they have read, and recommended to the Institute of Engineering for acceptance, a thesis report entitled "3D FEM Based Service Life Evaluation of Geogrid Reinforced Flexible Pavements under Heavy Vehicle Loading in Combined Curvature Gradient Sections" submitted by Prashanna Shrestha in partial fulfillment of the requirements for the degree of Master in Geotechnical Engineering.

Supervisor:
Asst. Prof. Dr. Ram Chandra Tiwari
Department of Civil Engineering
IOE, Pulchowk Campus

External Examiner:
Er. Prabhat Kumar Jha
Department of Road, Ministry of Physical Infrastructure and Transport
Government of Nepal

Program Coordinator:
Asst. Prof. Dr. Bhim Kumar Dahal
M.Sc. in Geotechnical Engineering
Department of Civil Engineering
IOE, Pulchowk Campus

Date: 27 April, 2026

DECLARATION

I hereby declare that this study titled "**3D FEM Based Service Life Evaluation of Geogrid Reinforced Flexible Pavements under Heavy Vehicle Loading in Combined Curvature Gradient Sections"** is based on my original research work. Related works on the topic by other researchers have been duly acknowledged. I owe all the liabilities relating to the accuracy and authenticity of the data and any other information included hereunder.

Prashanna Shrestha

080/MSGtE/012

MSc in Geotechnical Engineering

Date: 27 April, 2026

ACKNOWLEDGEMENTS

The author wishes to express sincere gratitude to the supervisor, Asst. Prof. Dr. Ram Chandra Tiwari, for invaluable guidance, critical insight, and patient mentorship throughout the course of this research. The time devoted to reviewing manuscripts, discussing results, and shaping the scope of this work is deeply appreciated. I would also like to thank my external examiner, Er. Prabhat Kumar Jha for his valuable suggestions and guidance for the thesis work. I am also incredibly grateful to the Program Coordinator of MSc in Geotechnical Engineering, Asst. Prof. Dr. Bhim Kumar Dahal, Prof. Dr. Indra Prasad Acharya, Asst. Prof. Dr. Santosh Kumar Yadav, and Asst. Prof. Dr. Basanta Raj Adhikari, as well as the entire Geotechnical Engineering Department at Pulchowk Campus. They have played a pivotal role in expanding my perspectives and enhancing my academic journey.

Gratitude is also extended to Er. Aanchal Tiwari (Former M.Sc. student in Transportation Engineering, IOE, Pulchowk) and other faculty members of the Department of Civil Engineering, Pulchowk Campus, for their academic support and stimulating intellectual environment. The Department of Roads, Nepal, is acknowledged for providing the geometric design data and the cumulative standard axle load for the Pipalamod Lower section of the Prithvi Highway corridor.

The geotechnical laboratory testing was conducted with the assistance of laboratory staff at CMTL, their technical expertise and cooperation are gratefully acknowledged. Finally, the author acknowledges the unwavering support and encouragement of family and friends throughout the duration of this program.

Prashanna Shrestha

Msc. Geotechnical Engineering

080/MSGtE/012

ABSTRACT

Flexible pavements on horizontal curves in Nepal's hilly road network are subjected to a three-dimensional loading state with vertical tyre loads, outward centrifugal force from vehicle movement, and longitudinal tangential traction from acceleration that is not represented in current IRC 37 based design procedures. This unconservative loading assumption contributes to very high rates of rutting and fatigue cracking observed at curved sections along corridors such as the Prithvi Highway. This study evaluates the structural response of geogrid reinforced curved flexible pavement at the Pipalamod Lower site on the Prithvi Highway (R = 32 m, e = 2.50%, G = 6.14%) which is selected on the basis of the tightest horizontal curvature among other grouped sections, a subgrade CBR of 5.86% (satisfying the DoR criterion of CBR > 5%), and a cumulative design traffic of 145 MSAL obtained from the Department of Roads. Geotechnical properties were determined from systematic laboratory testing. Pavement layer thicknesses were designed for 145 MSAL using IITPave under (IRC:37-2018). The design vehicle is a rear tridem axle 420 kN heavy commercial truck (v_0 = 9.5 m/s, a = 0.5 m/s^2) with rear axle loads of 105 kN and forward axle loads of 70 kN per axle. Three geogrid placement configurations asphalt base interface (BA), base subgrade interface (SB), and both interfaces simultaneously (SB+BA) were evaluated at three axial stiffness levels (EA =300, 600, 800 kN/m). Two critical pavement response parameters were monitored which are ε_{long} at bottom of asphalt and ε_{zz} subgrade's top. Strain ratio quantified reinforcement benefit. Fatigue life and rutting life were computed for each configuration for all stiffness. Results show that the cumulative loads designed for the straight road sections is insufficient for the horizontal sharp curves with longitudinal gradient. Geogrids can compensate the reduced life due to the curvature effects where BA+SB dual layer placement achieves the highest reductions in asphalt fatigue parameters reducing Elong by up to 25.86% and 21.17% for ε_{zz} relative to the unreinforced pavement in Pipalamod Lower site. If the single layer is to be used, BA configuration is optimal for the fatigue and SB configuration is optimal for rutting. Geogrid stiffness also has considerable sensitivity meaning increasing stiffness increases the strain reduction capacity in both fatigue and rutting criteria.

Keywords: Flexible Pavement; Geogrid; Centrifugal Force; Tangential Force; Pipalamod Lower; Horizontal Curvature; Longitudinal Gradient.

TABLE OF CONTENTS

LIST OF FIGURES

LIST OF TABLES

ABBREVIATIONS AND ACRONYMS

ABBREVIATIONS

3D FEM	: Three-Dimensional Finite Element Method
BA	: Asphalt-Base Interface Geogrid Placement
BA+SB	: Dual Layer Geogrid (both interfaces)
BoA	: Bottom of Asphalt Layer
CBR	: California Bearing Ratio
CRRI	: Central Road Research Institute (India)
DBM	: Dense Bituminous Macadam
DoR	: Department of Roads, Nepal
EA	: Axial Stiffness of Geogrid (kN/m)
EALF	: Equivalent Axle Load Factor
ESALs	: Equivalent Standard Axle Loads
FEM	: Finite Element Method
GSB	: Granular Sub-Base
IRC	: Indian Roads Congress
MC	: Mohr-Coulomb (Constitutive model)
MSAL	: Million Standard Axle Loads
OMC	: Optimum Moisture Content
SB	: Base-Subgrade Interface Geogrid Placement
SLR	: Service Life Ratio
ToS	: Top of Subgrade Layer
UCS	: Unconfined Compressive Strength
VDF	: Vehicle Damage Factor
WBM	: Water Bound Macadam

ACRONYMS

a	: Vehicle longitudinal acceleration
c'	: Effective cohesion of soil
e	: Superelevation rate
E	: Young's modulus
EA	: Geogrid axial stiffness
ε_{long}	: Tensile strain at longitudinal direction
ε_{xx}	: Longitudinal cartesian strain at BoA
ε_{yy}	: Transverse cartesian strain at BoA
ε_{zz}	: Vertical compressive strain at ToS
ε_1	: Principal compressive strain at ToS
F_c	: Centrifugal force
F_t	: Tangential traction force
G	: Longitudinal gradient
g	: Gravitational acceleration
M	: Vehicle mass
M_r	: Resilient modulus
N_f	: Fatigue life
N_R	: Rutting life
R	: Horizontal radius of curvature
v	: Vehicle speed
W	: Carriageway width
γ_{unsat}	: Unit weight (unsaturated)
γ_{sat}	: Unit weight (saturated)
ν	: Poisson's ratio
ω	: Angular velocity
w_{0_G}	: Without geogrid
α	: Angle between points of tyre
w	: Water content

2D	: Two dimensional
3D	: Three dimensional
φ, ϕ	: Angle of internal friction
ψ	: Dilatancy angle

1 INTRODUCTION

1.1 Background

Road infrastructure is the backbone of national development in Nepal which is a landlocked country of topographic diversity. The road network is the primary tool through which agricultural product, construction materials, essential goods, and emergency services are transported across a population of approximately 30 million people (Pokharel et al., 2020). As of 2023, Nepal's Department of Roads manages a strategic road network exceeding 14,000 kilometers which is surfaced with flexible bituminous pavement. Despite of the current investment, premature pavement deterioration remains a costly challenge with rutting, fatigue cracking, and structural deformation widely observed particularly on roads traversing hilly corridors (Wang & Al-Qadi, 2010).

Flexible pavements are layered structures with a wearing course of asphalt, base course of granular layer, natural subgrade designed to transmit traffic loads progressively to the foundation soil while limiting critical stresses and strains to acceptable levels (Kwon et al., 2008). The structural design of these pavements in Nepal follows the Indian standard for the mechanistic empirical framework controlling tensile strain at the bottom of the bituminous layer for the fatigue cracking and vertical compressive strain at the top of the subgrade for the rutting (Indian Roads Congress, 2018)(IRC 37, 2018).

In the hilly terrain, horizontal curves are an unavoidable feature. Sharp curves are particularly prevalent on the Prithvi Highway where curved sections are necessary to gain or lose elevation. Horizontal curves alter the loading conditions experienced by the pavement and as a vehicle negotiates a curve, centrifugal acceleration generates an outward lateral force that adds to the vertical tyre load producing a combined multi-directional stress state not captured by the axisymmetric load models on which most pavement design procedures including Indian standards are based.

1.2 Flexible Pavement Distress in Nepal's Hilly Road Network

Field observations across Nepal's hilly road network consistently reveal that curved sections suffer high rates of pavement distress compared to straight sections. Rutting is severe on curves where centrifugal loading concentrates stresses on the outer wheel path. Fatigue cracking is frequently observed near the inner edges where the superelevated cross section is thinnest. Pavement condition assessments from 2014 to 2023 identified widespread and accelerating pavement deterioration with structural distress modes where rutting and fatigue dominate (Bennett & Pedersen, 2023).

The dominant heavy vehicle type on these corridors includes multi-axle commercial trucks carrying gross vehicle weights that generate the most severe pavement responses. The combination of weak subgrade CBR, sharp horizontal curvature, steep longitudinal grades, and heavy multi-axle vehicle loading represents the critical design scenario for Nepal's hilly road network.

1.3 Geogrid Reinforcement as a Structural Enhancement Strategy

Geosynthetic geogrid reinforcement has emerged as a cost effective and well proven technique for improving flexible pavement structural performance on routes with weak subgrade conditions. Geogrids provide tensile reinforcement through three mechanisms which are lateral restraint of granular particles through interlocking and confinement, tensioned membrane vertical support and improved load distribution (Giroud & Noiray, 1981; Gu et al., 2017; Pandey et al., 2012).

Despite this strong evidence, the adoption of geogrid reinforcement in Nepal's road construction program has been limited and design guidelines for geogrid reinforced pavements remain absent from the DoR's published standards. The effectiveness of geogrid reinforcement in curved pavement sections where three-dimensional vehicle loading is different from the axisymmetric loading assumed in straight road studies has never been systematically investigated.

1.4 Research Gaps and Problem Statement

- The structural design of flexible pavements in Nepal is based on the assumption that traffic loading is a vertically applied axisymmetric force on a horizontal, straight road surface. This assumption fails to capture the actual loading conditions experienced by pavements on horizontal curves.
- Only few published study has evaluated how different geogrid placement locations and axial stiffness values affect the critical structural responses of a curved flexible pavement section subjected to centrifugal and tangential forces generated by a moving heavy multi-axle vehicle.
- Previous studies in Nepal have not considered site specific fatigue and rutting life predictions under the actual vehicle loading conditions in curvature gradient flexible pavements.

1.5 Objectives

The main aim is to analyze the structural response of the geogrid reinforced curved flexible pavement at the Pipalamod Lower site under three-dimensional loading of a moving heavy vehicle.

The specific objectives are:

- To develop accurate 3D FEM models at real curved sites of Pipalamod lower in PLAXIS 3D.
- To quantify the effects of geogrid placement (3 configurations) and stiffness (3 levels) on critical pavement responses (300, 600, 800 kN/m).

1.6 Scopes

- Addresses the effects of curvature and gradient of Pipalamod Lower site.
- Three geogrid configurations: BA, SB, BA+SB and four stiffness levels of 300, 600, 800 kN/m.
- Two critical strain parameters, ε_{long} at the bottom of the asphalt and ε_{zz} at the top of the subgrade were focused.
- Fatigue (N_f) and rutting (N_r) life computed using IRC:37-2018
- Heavy axles vehicle is moved in the horizontal curved section with gradient.
- Comparison of the obtained pavement life with the adopted designed life for the horizontally curved flexible pavement with longitudinal gradient.

1.7 Limitations

- The Mohr-Coulomb model does not capture viscoelastic behavior of asphalt.
- The quasi-static multi-phase approach does not represent exact dynamic inertial effects.
- Vehicle movement is limited to single pass simulation due to resource limitation for huge number of passes.
- Linear correlation is used to convert strains from one axle load to another.

2 LITERATURE REVIEW

2.1 Flexible Pavement Behavior on Horizontal Curves

The flexible pavement behavior is actually complex. Many studies have tried to incorporate its behavior in many ways. The study focuses mainly on the structural behavior of flexible pavements under heavy commercial vehicles, the use of geogrids as a reinforcement, the application of three-dimensional finite element modelling to capture pavement response, and the effects which occur when a road segment carries both a horizontal curve and a longitudinal gradient. Each of these areas has its own body of literature.

2.1.1 Effect of longitudinal gradient

The traditional pavement design assumption is that the wheel load is purely vertical but it fails on long, steep grades. On an uphill segment, a heavy truck climbs slowly with high engine torque, and on a downhill segment it brakes. In both cases, high horizontal traction force is transmitted to the surface in addition to the vertical wheel load. Guo et al. (2021) analyzed asphalt pavements with semi rigid bases on steep longitudinal slopes and showed that the horizontal traction has a strong effect on the distribution of shear stress within the layered system. They observed that gradient and slope length have a minor effect on shear stress, but that the magnitude of the horizontal force is a function of these geometric parameters through truck speed.

2.1.2 Effect of horizontal curvature

On horizontal curves, the lateral component of tire pavement traction which is generated by centripetal acceleration applies a shear force onto the vertical wheel load. The implication is that curved sections experience a fundamentally different stress conditions from straight tangents with the upper bituminous layers carrying a much share of the shear. Luo et al. (2023) have reported that changing the radius of a horizontal curve has a more significant effect on horizontal shear stress than changing the longitudinal slope alone and very tight curves can drive the shear stress in the wearing course beyond the strength of the binder leading to early life tearing and longitudinal top to down cracking.

2.1.3 Combined curvature and gradient sections

Real highway alignments in mountainous and hilly country rarely separate horizontal curvature from longitudinal grade. The combined-geometry case which is a horizontal curve combined with a longitudinal gradient. The asphalt pavement on combined sections is influenced by multiple factors. Zheng et al. (2017)gave a similar conclusion in the curved and sloped ramp simulation where the interaction between the longitudinal friction force on the slope and the lateral force on the curve produced a pattern which doesn't occur alone in the vertical loading. The available evidence focuses on combined curvature-gradient sections as the locations of greatest risk on a flexible pavement section. They concentrate slow moving heavy traffic, sustain large multi-directional surface tractions, and accumulate longer load durations because trucks cannot maintain design speeds.

2.1.4 Pavement performance in hilly and mountainous terrain

The Indian Roads Congress (2018)and the Nepal Department of Roads' Pavement Design Guidelines (DoR, Nepal) both assign higher vehicle damage factors (VDFs) to two-axle and three-axle trucks operating in hilly terrain than on plains.

However, the VDF adjustment is an assumed correction which does not differentiate between damage on a straight climb and damage on a curved climb of the same gradient nor does it account for the concentration of distress that results from braking and steering on combined sections. The literature on geogrid-reinforced pavements in such terrain is correspondingly thin that means the most field and laboratory studies have been performed on flat sections.

2.1.5 Geometric design of horizontal curves

The horizontal curves geometric design in flexible pavements is governed by the connection between design speed, radius of curvature, superelevation, and lateral friction. As a vehicle travels a horizontal curve, an outward centrifugal force is generated whose magnitude is proportional direct to vehicle speed squared and is proportional inversely to the curvature radius (Fitzpatrick & Kahl, 1992). The fundamental relationship is expressed as $P = \frac{Wv^2}{gR}$, W is the vehicle weight (kN), v is the speed of vehicle (m/s), g is 9.81 m/s^2, and R is the radius of curvature(m)(Abdulhafedh, 2019; Himes & Donnell, 2014). To counteract centrifugal effects, superelevation is provided throughout the curve, and the design equilibrium condition requires $e + f = \frac{V^2}{127R}$, where e is the superelevation rate and f is the lateral friction coefficient (Abdulhafedh, 2019). Wang et al. (2014) demonstrated through 3D FEM that vehicle maneuvering on curved sections produces lateral shear forces at the tyre pavement interface that substantially alter the distribution of critical strains in the pavement structure.

2.1.6 *IIT Pave and mechanistic empirical pavement design*

The IITPave software developed by the Central Road Research Institute (CRRI) of India implements the IRC 37 mechanistic empirical design framework. Polisetti & Baadiga (2025)validated the combined IIT Pave and PLAXIS 3D workflow by demonstrating close agreement between computational predictions and field plate load test data across subgrade CBR values of 2%, 5%, and 10%.

2.2 Vehicle Dynamics and Force Mechanics on Curved Road Sections

The vehicle dynamics and force mechanics on curved road sections are discussed below.

2.2.1 *Centrifugal force in curved road travel*

When a vehicle travels along a horizontal curve, each wheel follows a concentric circular arc of a distinct radius generating a unique centrifugal force which is $Fc = \frac{Mv^2}{R} = M\omega^2 R$, where $\omega = \frac{v}{R}$ is the angular velocity (Wowk, 2015). IRC:37-2018 and Mehta et al. (2021)confirm that centrifugal force increases with the square of vehicle speed and decreases with radius making it most critical on sharp curves at high speed. Wang et al. (2014) confirmed using 3D FEM that surface friction forces during vehicle maneuvering produce shear stresses at the pavement surface that significantly increase subsurface tensile strains in the asphalt layer.

2.2.2 *Tangential force due to vehicle acceleration*

A vehicle accelerating along a curved path exerts a tangential traction force $F_t = M \times a$ on the pavement surface. When resolved into global Cartesian coordinates for a vehicle at angular position α along the circular path, the centrifugal and tangential forces can be resolved in to X and Y directions as (Beer et al., 2019):

$$F_x = F_c \cos(\alpha) - F_t \sin(\alpha) \quad (1)$$

$$F_y = F_c \sin(\alpha) + F_t \cos(\alpha) \quad (2)$$

The above equation “Equation (1)” and “Equation (2)” is obtained from Beer et al. (2019).

“Equation (1)” is the resolved force in x-direction and “Equation (2)” is the resolved force in Y direction.

This vector decomposition is consistent with classical mechanics for circular motion and has been employed in pavement vehicle interaction studies (Beskou & Muho, 2023)

2.2.3 Multi-axle heavy vehicle loading

Heavy commercial vehicles are the primary cause of structural distress in flexible pavements. Elnashar et al. (2019)confirmed using a full 3D FE model that pavement responses under a moving multi axle truck are significantly higher than those predicted by static analysis at higher vehicle speeds.

2.3 Geogrid Reinforcement in Flexible Pavements

For the flexible pavements geogrid reinforcing mechanisms have been discussed by many literatures. Webster (1992) in his Waterways Experiment Station report on light-aircraft pavements showed that biaxial geogrids placed at the base-subgrade interface allowed the unbound layer thickness to be reduced for an equivalent number of load passes. These early experimental findings were made by Perkins (1999) in a two part review that has become a standard reference. Perkins (1999) followed with large scale instrumented box tests in which surface deformation, base and subgrade stresses, and strains in the geosynthetic itself were measured directly. The reinforced sections consistently showed reduced lateral spreading of the base aggregate and a smaller permanent surface rut.

2.3.1 Mechanisms of geogrid reinforcement

Geogrids are polymeric geosynthetics used as reinforcing elements within pavement layers. The primary reinforcement mechanisms by Haas et al. (1988) are:

1. Lateral restraint of granular particles through interlocking and confinement.
2. Tensioned membrane support, which provides a vertical reaction component against downward deformation.
3. Improved load distribution that reduces the stress transferred to the subgrade (Giroud & Noiray, 1981). The tensile modulus or axial stiffness (EA, in kN/m) is the most critical property governing reinforcement efficiency.

2.3.2 Effect of geogrid placement location

Using PLAXIS 2D demonstrated that placing geogrid at the asphalt and base interface leads to the reduce in horizontal fatigue strain at the bottom of the asphalt's layer while placing it at the base subgrade interface produces the largest reduction in vertical compressive rutting strain at the top of the subgrade with vertical loading Faheem & Hassan (2014).

Ibrahim et al. (2017) did triaxial compression tests with three subgrade soils which reported that the maximum reinforcement effect was obtained when the geogrid was placed at roughly 25 % of the layer height from the bottom. The recent PLAXIS 3D parametric study of Chhetri & Deb (2024) brought these strands together and showed that the optimum position depends systematically on subgrade stiffness: at H/4 from the top of the granular layer for very weak subgrades (CBR < 3 %), at H/3 for intermediate subgrades, and at the base sub-base interface for stiffer subgrades. Despite the variation among studies, there is broad agreement that the reinforcement is essentially ineffective if it is placed outside the tensile strain zone which is the geometric reason for the thickness dependent recommendations.

2.4 Finite Element Modelling of Flexible Pavements

Finite element modeling is the best tool to do the numerical analysis of the problem which reduces the manual computation in many ways.

2.4.1 Two-dimensional and three-dimensional approaches

Two-dimensional axisymmetric FE models are still common because they are computationally inexpensive and capture vertical stresses and surface deflections reasonably well. Calvarano et al. (2017) reported that 2D plane strain models predict rut depth within roughly 2 % of a fully 3D model for a single static wheel which helped to justify the continued use of 2D approaches in some design studies. Three-dimensional models become important when the wheel moves, when the load distribution is non-axisymmetric, when the structure is reinforced by an embedded sheet, or when the road geometry is different from straight. Zaghloul & White (1993) were among the first to demonstrate a 3D ABAQUS analysis of a moving load on a flexible pavement with the results that match to field strains.

2.4.2 FE studies on geogrid-reinforced flexible pavements

Researcher Abu-Farsakh et al. (2014) reported the early 3D FE studies of geosynthetic reinforced flexible pavements using ABAQUS which modelled the geogrid as embedded membrane elements with frictional contact to the surrounding aggregate. Their parametric study showed that including the geogrid lowered the maximum ε_{long} at bitumen layer bottom and ε_{zz} at the top of the subgrade, and that the magnitude of these reductions depended strongly on the tensile modulus of grid. Abu-Farsakh et al. (2014) extended this approach by combining the FE response model with mechanistic empirical damage models to estimate the service life extension provided by various geogrid configurations. Their results suggested that, for a given pavement structure, geogrid reinforcement reduced surface rutting by up to 35 % and increased pavement service life by a factor of two to four and also the larger improvements observed for thinner bases over weaker subgrades. Calvarano et al. (2017); Leonardi & Suraci (2022) developed Abaqus/CAE 3D models in which the geogrid was modelled with shell elements embedded in a Drucker Prager unbound layer.

Three-dimensional finite element analysis has become the best tool for investigating pavement structural responses under complex loading conditions. PLAXIS 3D employs 10 noded tetrahedral elements that provide a second order displacement field widely recognized as providing an accurate balance between computational efficiency and numerical accuracy for geotechnical and pavement problems (Brinkgreve, 2019). Cardenas & Al-Qadi (2024) demonstrated that combined roughness induced dynamic loading and directional maneuvering produce strains that cannot be predicted by conventional static models. Beskou & Muho (2023)confirmed that vehicles modelled with acceleration and deceleration produce measurably different strain histories compared with constant speed simulation.

2.4.3 Geogrid reinforcement in 3D FEM using PLAXIS 3D

Polisetti & Baadiga (2025)used PLAXIS 3D to evaluate geogrid reinforcement across subgrade CBR values of 2 %, 5 %, and 10 % and geogrid stiffnesses of 400, 800, 1200, and 1500 kN/m validating against field plate load test data. Their results demonstrated that stiffer geogrids systematically reduce both settlement and critical strains with greater improvement on weaker subgrades. Gu et al. (2017)used ABAQUS to characterize the lateral confinement and vertical membrane effect of geogrids in flexible pavements validating their model against full scale soil tank test data.

2.4.4 Summary of geogrid studies and research gap

Table 2.1 summarizes selected literature studies on geogrid reinforced flexible pavement FEM analysis. The review reveals that while geogrid reinforcement of straight flexible pavement sections has been extensively studied using both 2D and 3D FEM. There is a distinct lack of research on geogrid reinforced curved pavement sections with longitudinal gradient subjected to a fully three-dimensional moving multi-axle heavy vehicle load including centrifugal and tangential force components.

Table 2.1: Geogrid-reinforced flexible pavement FEM studies

Author(s) & Year	Software	Geogrid Location	Key Finding
(Faheem & Hassan, 2014)	PLAXIS 2D	Asphalt-Base; Base-Subgrade	Asphalt-base placement reduces fatigue strain; base-subgrade reduces rutting strain
(Gu et al., 2017)	ABAQUS	Mid base course	Lateral confinement and membrane effect explicitly characterized and validated
(Correia & Zornberg, 2018)	PLAXIS / FE	Asphalt-Base Interface	14% (cyclic) and 22% (static) reduction in asphalt tensile strain
(Chhetri & Deb, 2024)	FE	Within base course	Significant reduction in surface deformation and subgrade stress on soft subgrade
(Sivaprakash et al., 2025)	PLAXIS 2D	Both interfaces	Dual-interface reinforcement superior to single for both fatigue and rutting
(Polisetti & Baadiga, 2025)	PLAXIS 3D	Optimized depth	Higher stiffness reduces critical strains; IITPave PLAXIS 3D workflow validated against field data

2.5 Automation in FEM Pre-Processing and Post-Processing

The PLAXIS 3D Remote Scripting API which is a Python-based HTTP interface allows external scripts to interact with the software to create geometry, assign properties, define phases, and extract output (Hemeda, 2022). In the present study, Python automation was employed at both pre-processing stage (curved path point load coordinates and dynamic force assignments) and post-processing stage (systematic extraction of pavement response parameters) representing a methodological advancement over existing pavement FEM studies that rely on manual model construction and results extraction. Different input and output commands are used for the python scripting.

2.6 Strain ratio, Fatigue and Rutting

Term Strain ratio is introduced for the parametric comparison which is defined as the ratio of the ε_{zz} and ε_{long} at the subgrade's top and asphalt base respectively in the unreinforced condition to the corresponding strain in the reinforced condition. Similarly, the formula for the fatigue and rutting life is mentioned in the study by Indian Roads Congress (2018). According to the study, the fatigue and rutting life are calculated as below:

Fatigue life prediction: The following empirical relationship linking the number of load reptations to fatigue failure with the tensile strain at the bottom of the asphalt layer and the asphalt stiffness modulus Indian Roads Congress (2018) (IRC:37-2018).

$$N_f = 0.5161 * C * 10^{-4} * \left[\frac{1}{\varepsilon_t}\right]^{3.89} * \left[\frac{1}{M_{Rm}}\right]^{0.854} \quad (3)$$

In "Equation (3)" by Indian Roads Congress (2018) , N_f denotes the load applications required to propagate fatigue cracking across the wheel-path area, ε_t is the repeatedly applied horizontal tensile strain at the base of the asphalt layer, and ε_1 is the asphalt stiffness modulus in N/mm^2.

Rutting life prediction: Indian Roads Congress (2018) expressed the corresponding rutting life as a function of the compressive strain as by Indian Roads Congress (2018) in vertical direction transmitted to the surface of the subgrade:

$$N_r = 1.4100 * 10^{-8} * \left[\frac{1}{\varepsilon_v}\right]^{4.5337} \quad (4)$$

In "Equation (4)" by Indian Roads Congress (2018), N_r is the number of load applications corresponding to the onset of rutting failure, and ε_v is the vertical compressive strain at the top of the subgrade.

3 STUDY AREA AND DATA

Pipalamod Lower located on the Prithvi Highway was selected as the sole study site for this analysis on the basis of three criteria established:

- The tightest horizontal curvature among candidate sections (R = 32 m), representing the most critical combined centrifugal and tangential loading condition.
- Subgrade CBR of 5.86%, satisfying the (DoR, Nepal) requirement that CBR must exceed 5% for structural analysis.
- Representative of the hilly corridors of Nepal.

The site plan of the Pipalamod Lower section derived from the Department of Roads survey report is shown in Figure 3.1. Figure 3.2 shows the section considered for study.

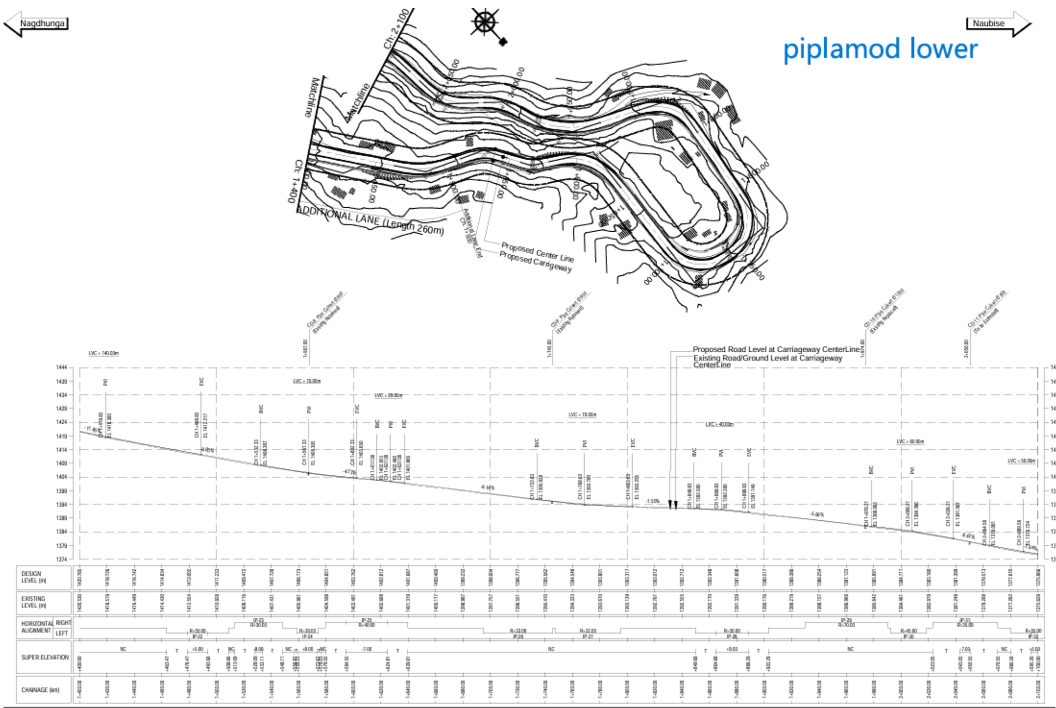

Figure 3.1: Pipalamod lower curved section (DoR survey report)

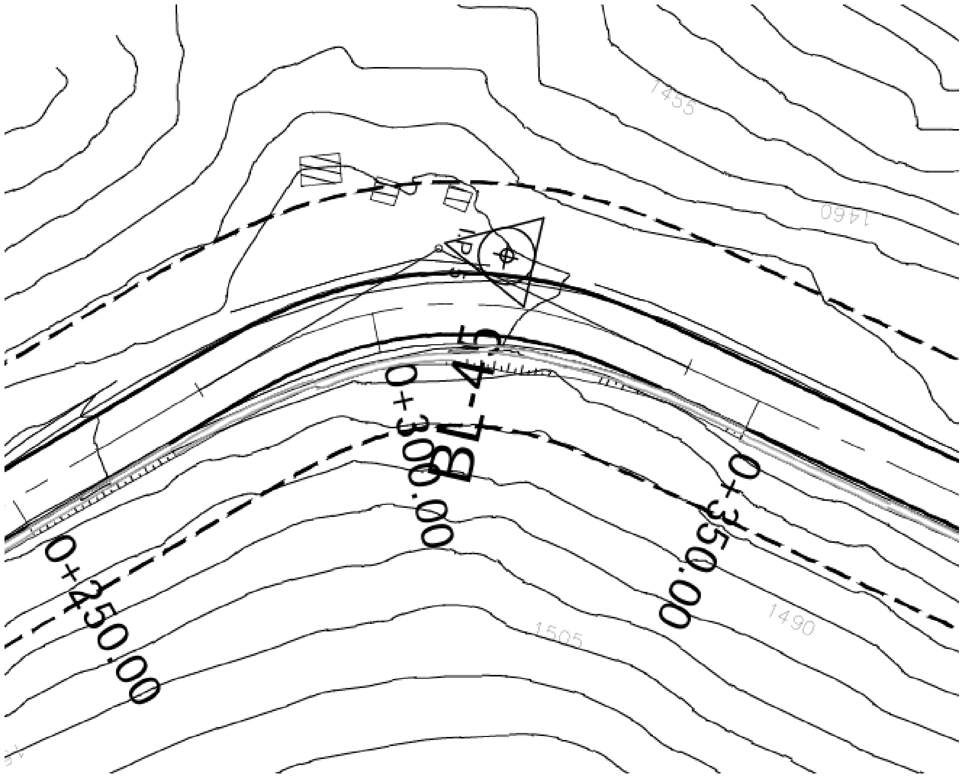

Figure 3.2: Section considered for pipalamod lower site

Table 3.1: Geometric parameters of site

Site	Radius (m)	Width (m)	Superelevation (%)	Long. Grade (%)
Pipalamod Lower	32	9	2.50	6.14

Table 3.1 provides the information about the geometric parameters used for the geometry construction of the pavement which is adopted from the design report provided by the Department of Road(DoR), Nepal. Initially, the geometric data from five sites were extracted. Later, only one was selected which is Pipalamod Lower.

Figure 3.3 is put to show the section of the pipalamod lower considered for the study. From the figure, it can be seen that Pipalamod Lower has the tightest curvature where the effects of the centrifugal force and tangential force can be greatly seen.

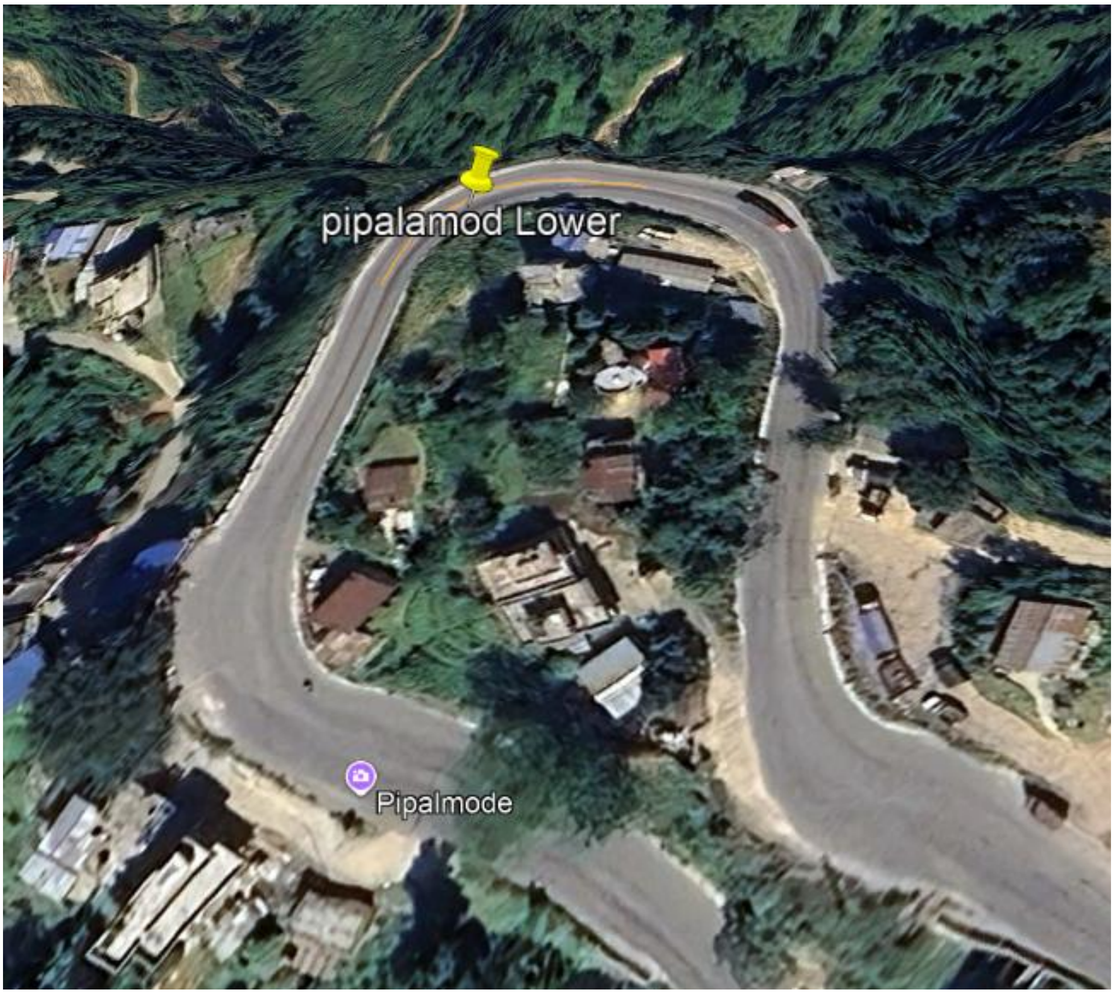

Figure 3.3: Pipalamod lower section from google earth pro

4 METHODOLOGY

To achieve the required objectives, six steps of methodology was adopted which can be visualized in the methodology flowchart of Figure 4.1

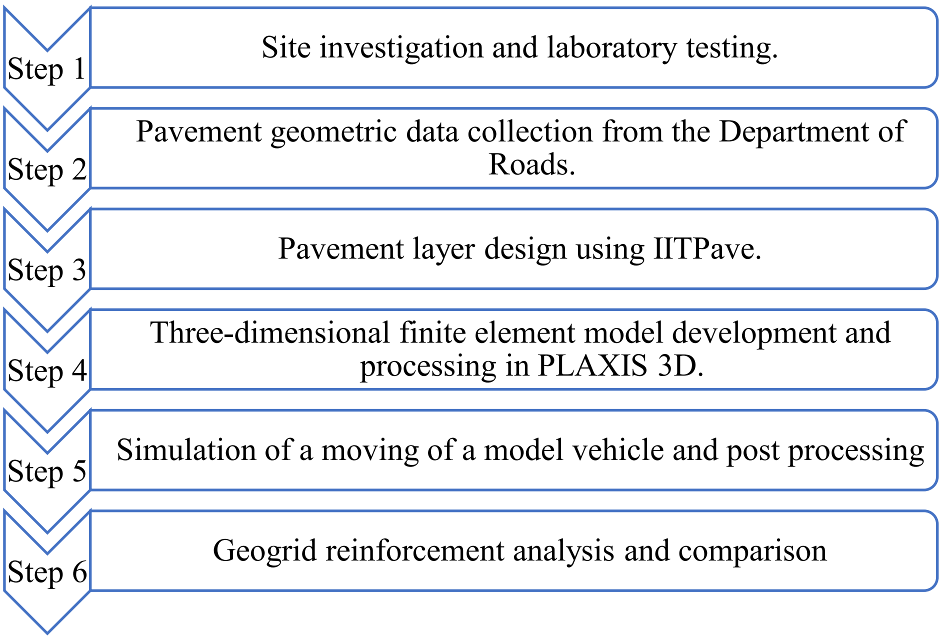

Figure 4.1: Methodology flowchart

The overall methodology was arranged so that each step would follow the next, which starts from field reconnaissance and ends with the comparative analysis of the different geogrid configurations. The reason behind organizing the work in this sequence was to ensure that field data, laboratory results and design parameters were all along with each other before any numerical model was created. Errors that come at the data collection stage will affect throughout the process.

Both experimental and computational parts were used in this work. The experimental part provided the material parameters that show the actual ground conditions at the chosen site while the computational side allowed those parameters to be tested under traffic loading conditions that would be difficult or not safe to create in the field. By bringing these two sides together, it became possible to study the influence of geogrid reinforcement on a curved hill road section without disturbing live traffic on the highway and to explore configurations that have not yet been physically constructed on the corridor.

4.1 Site Investigation and Laboratory Testing

The detailed investigation of five sites was done. Initially, the reconnaissance of the site was done. The criteria required to fulfill the site selection were focused on are radius, width, longitudinal gradient, site CBR, etc. Among them, Pipalamod lower site was selected based on its tight curvature, high longitudinal gradient, etc. Disturbed and undisturbed soil samples were collected from the Pipalamod Lower site following IS 2720 series procedures. The testing program determined all the required parameters for Mohr Coulomb material model. The laboratory investigation covered the following tests: Atterberg limits, specific gravity, compaction test/OMC, CBR, direct shear test, grain size analysis, unconfined compressive strength, and consolidation test (IS 2720-1, 1983; More et al., 2021). Table 4.1 summarizes the Mohr Coulomb parameters determined.

Table 4.1: Mohr coulomb parameters

Parameter	Symbol	Test Standard	Unit
Unit weight	γ	IS 2720 Part 2	kN/m^3
Cohesion	c'	IS 2720 Part 13	kPa
Friction angle	φ	IS 2720 Part 13	degrees
Young's Modulus	E	CBR (IRC 37)	MPa
Poisson's ratio	ν	Literature correlation	
CBR	CBR	IS 2720 Part 16	%

4.2 Pavement Geometry Data Collection

To obtain the required geometric properties of the selected site, reports from the Department of Road, Nepal was obtained containing the geometric properties of the site. The geometric data were thoroughly studied and adopted for the model creation. Following geometric properties were obtained.

Site: Pipalamod Lower

Radius(m): 32

Width(m): 9

Superelevation: 2.50 %

Longitudinal gradient: 6.14 %

4.3 Pavement Layer Design Using IITPave

The cumulative design traffic for Pipalamod Lower was obtained directly from the Department of Roads, Pulchowk, Nepal as 145 MSAL. All IITPave structural designs are based on this 145 MSAL for 15 years design period. Structural design was carried out using IITPave software implementing the IRC 37 mechanistic empirical framework. The subgrade CBR of 5.86% was used to define subgrade bearing capacity, and the layer thicknesses and associated resilient moduli satisfy the fatigue and rutting strain criteria of (IRC:37-2001) Indian Roads Congress (2018) for 145 MSAL. Table 4.2 presents the design outputs obtained from the IITpave software.

Table 4.2: Pavement layers and properties

Layer	Thickness in (mm)	Modulus in (MPa)	Poisson's Ratio	Material
Bituminous (DBM)	200	3000	0.35	Dense Bituminous Macadam
Base Course	420	165.37	0.35	WBM/Crushed Stone Base
Subgrade (natural)	5000	54.57 (Mr)	0.35	Silty clay

4.4 Three-Dimensional Finite Element Model Development

4.4.1 Modelling platform and element type

All numerical simulations were performed using PLAXIS 3D. The soil continuum was discretized using the 10-noded tetrahedral element available in PLAXIS 3D. This element has quadratic displacement interpolation, four corner nodes, six mid-side nodes, and four Gauss points for numerical integration (Brinkgreve, 2019). The use of 10-noded elements in PLAXIS 3D for pavement analysis is consistent with recent literature practice (Polisetti & Baadiga, 2025).

4.4.2 Geometry construction in PLAXIS 3D

The three-dimensional pavement geometry was constructed in PLAXIS 3D using the geometric parameters from the DoR, Nepal design reports for Pipalamod Lower. Three distinct horizontal layers subgrade, granular base course, and bituminous asphalt surfacing were defined. All layer interfaces were modelled as fully bonded connections. The loft feature was used for the complicated surface creation. Geogrid elements were inserted as zero thickness membrane elements at the specified interface planes in the reinforced model variants which is modeled as linear elastic. Figure 4.2 shows the complete geometry along with the point load setup. Bottom blue layer is subgrade; green layer is base and top yellow layer is asphalt.

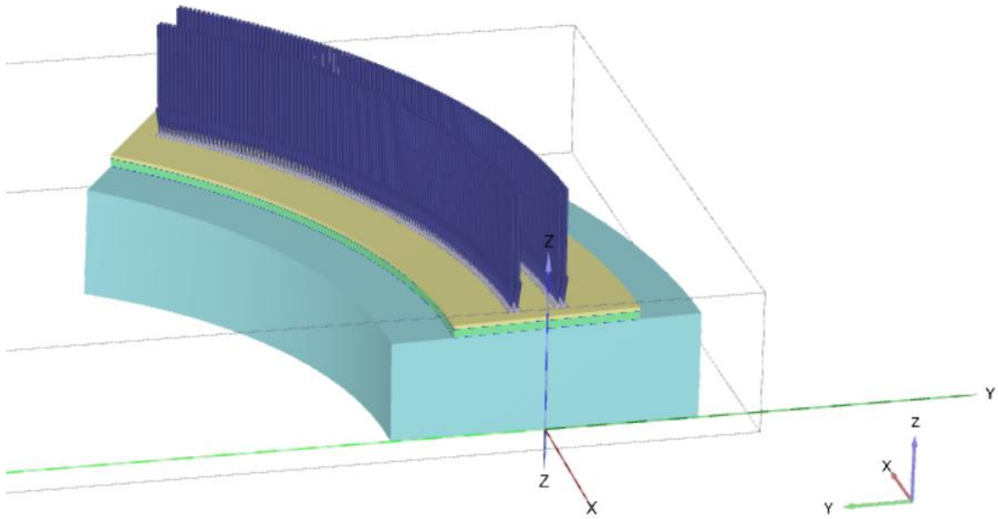

Figure 4.2: Geometry and the point load setup

4.4.3 Material modelling and properties assignment

The subgrade and granular base course are modelled using the Mohr-Coulomb elastoplastic constitutive model, while the bituminous asphalt layer was modelled with a linear elastic material. Subgrade parameters were obtained from laboratory testing, while base and asphalt parameters were sourced from IITPave outputs where WBM (Water Bound Macadam) for granular base and DBM (Dense Bituminous Macadam) for asphalt layer were used. Geogrid elements were assigned linear elastic biaxial stiffness values of 300, 600 and 800kN/m. The properties of layers of materials of the model are shown in Table 4.3.

The model selected for the subgrade and granular base is Mohr-Coulomb. Since IRC is based on the linear elastic material model for the design of the flexible pavement for all layers, this study has focused on higher Mohr-coulomb material model. Every input to the model is backed by site specific test data rather than assumed values.

Table 4.3: Properties of different layers of materials

Subgrade	**Base (Water Bound Macadam) (IRC:19-2005)**	**Asphalt(Dense Bituminous Macadam) (IRC:37-2018)**
Unsaturated unit weight = 16.89 kN/m^3	22.6 kN/m^3	-
Saturated unit weight=19.47 kN/m^3	23.4 kN/m^3	23 kN/m^3
E=54.57e3 kPa	165.37e3 kPa	3000e3 kPa
c=17.56KN/m^2	2.5 kN/m^2	-
ϕ=30.96˚	42˚	-

4.4.4 Mesh generation and local coarseness refinement

The finite element mesh was generated using PLAXIS 3D's built in automatic meshing engine producing unstructured 10-noded tetrahedral meshes (Brinkgreve, 2019). A mesh sensitivity study was conducted after which the final mesh was selected at the configuration where further refinement produced less than 2 % change in critical strain values. The point loads were meshed very finely as the stress concentration occurs there heavily. The asphalt was modeled fine, base medium and subgrade was meshed coarse. Table 4.4 lists the local coarseness factors.

Table 4.4: Local coarseness factors implemented

Component	**Element Type**	**Coarseness Factor**	**Mesh Density**	**Justification**
Subgrade	10-noded tetrahedra	1.0 (coarsest)	Standard	Diffuse stress state at depth; coarser mesh reduces element count without loss of accuracy

Granular base course	10-noded tetrahedra	0.75	Medium-fine	Transition zone; moderate refinement captures base-subgrade interaction
Bituminous asphalt layer	10-noded tetrahedra	0.5	Fine	High stress gradients under tyre contact; fine mesh required for accurate strain computation
Point load locations	10-noded tetrahedra	0.3 (finest)	Very fine	Maximum stress concentration zone; very fine mesh essential for accurate extraction of critical strains
Geogrid surfaces	10-noded tetrahedra	0.3 (finest)	Very fine	For accurate extraction of critical strains

The mesh statistics for the Pipalamod Lower model are: Total elements: 23935; Total nodes: 54926; Total phases: 88 (Phases 3-88 for vehicle traversal).

4.4.5 Boundary conditions, calculation type and phase sequence

The boundary's conditions which is applied to the PLAXIS 3d model are: bottom face (fully fixed: Ux = Uy = Uz = 0 which gives the rigid base assumption), side faces were transverse (normally fixed, roller boundary) to prevent the lateral shift of particles, side faces longitudinal (normally fixed, roller boundary), and top surface (free point loads applied at tyre contact coordinates). Figure 4.3Figure 4.3 is the boundary conditions which are adopted in the model which was taken from the study (Brinkgreve, 2019).

All calculation phases employed the plastic analysis calculation type and staged construction loading type in PLAXIS 3D using the Newton-Raphson incremental iterative procedure (Brinkgreve, 2019).The initial phase used the K0 procedure to establish the geostatic stress state. Subsequent phases activated pavement layers which are subgrade and base. The reset to displacement was adopted on phase 2 to balance the displacement due to the placement of subgrade, base and asphalt layer. Later, it was followed by 86 vehicle loading phases (Phases 3-88) representing the vehicle traversing the curve to see the effects of only vehicle travel.

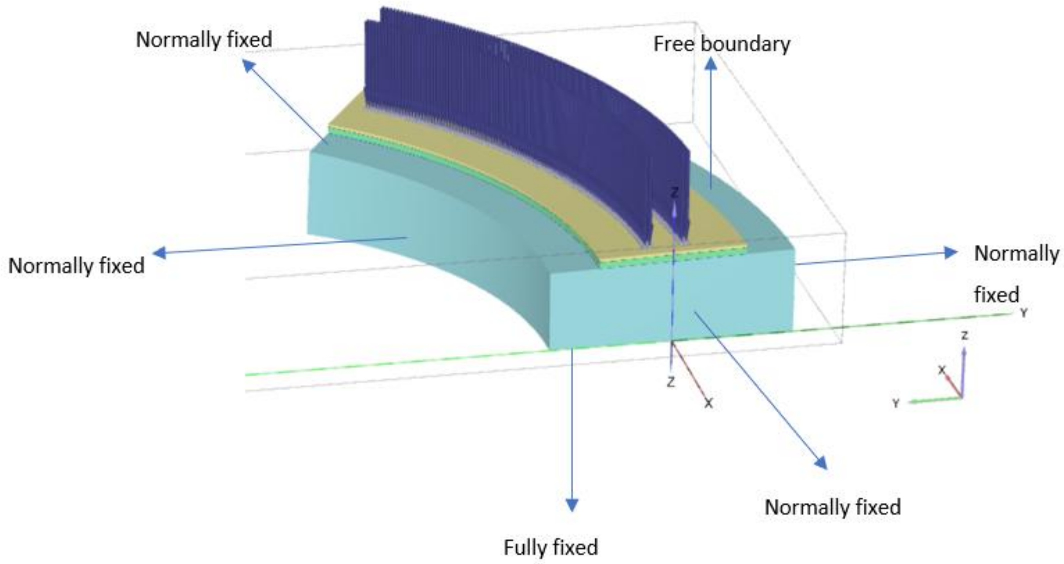

Figure 4.3: Boundary condition

4.5 Simulation of Moving a Model Vehicle and Post Processing

The design vehicle is a LPT 4225.T BSVI COWL 10*2 tridem rear axle heavy vehicle (TATA) shown in Figure 4.4 with gross vehicle weight (GVW) commercial truck representative of heavily loaded goods vehicles commonly operating on the Prithvi Highway. The axle load distribution is two heavy rear axles each carrying 105 kN and three lighter forward axles each carrying 70 kN per axle. Table 4.5 summarizes the vehicle parameters. The Figure 4.5 displays the dimensions of the axle configurations of LPT 4225.T BSVI COWL 10*2 tridem rear axle heavy vehicle.

*Table 4.5: LPT 4225.T BSVI COWL 10*2 parameters*

Description	Parameters of Vehicle
Total axles	5
Gross vehicle weight (GVW)	42 tonnes (420 kN)
Last axle (rear)	105 kN
2nd last axle	105 kN
3rd, 2nd, 1st axles	70 kN each
Design speed (v_0)	9.5 m/s

Longitudinal acceleration (a)	0.5 m/s^2
Curve radius (Pipalamod Lower)	32 m
Loading phases	88 phases (Phase 3 to Phase 88)
Dimensions(mm) axle (1-2,2-3,3-4,4-5)	(2000, 3430, 1350, 1350) comprising wheel base 6780mm
Width of axle	2500 mm overall

*Figure 4.4: LPT 4225.T BSVI COWL 10*2 tridem rear axle heavy vehicle*

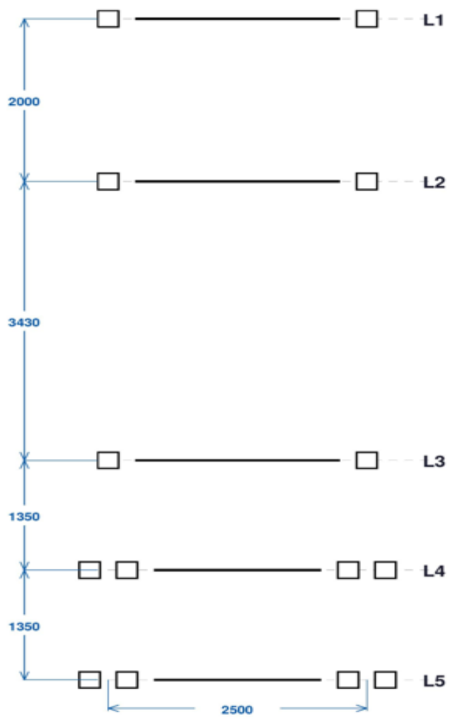

Figure 4.5: Dimension of vehicle(mm)

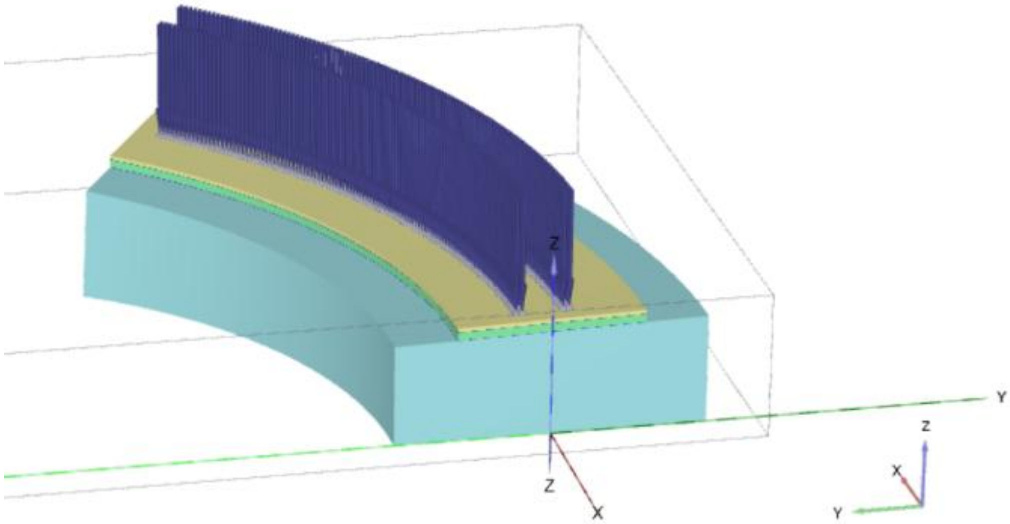

Figure 4.6: Whole pointed load setup

The whole pointed load which is later used to activate particular 14-point loads in different particular phase to simulate the moving vehicle is shown in Figure 4.6 and the Figure 4.7 to Figure 4.13 show the position of the vehicles at different positions which help to visualize the moving of the vehicle in the curved section of the pavement phase by phase.

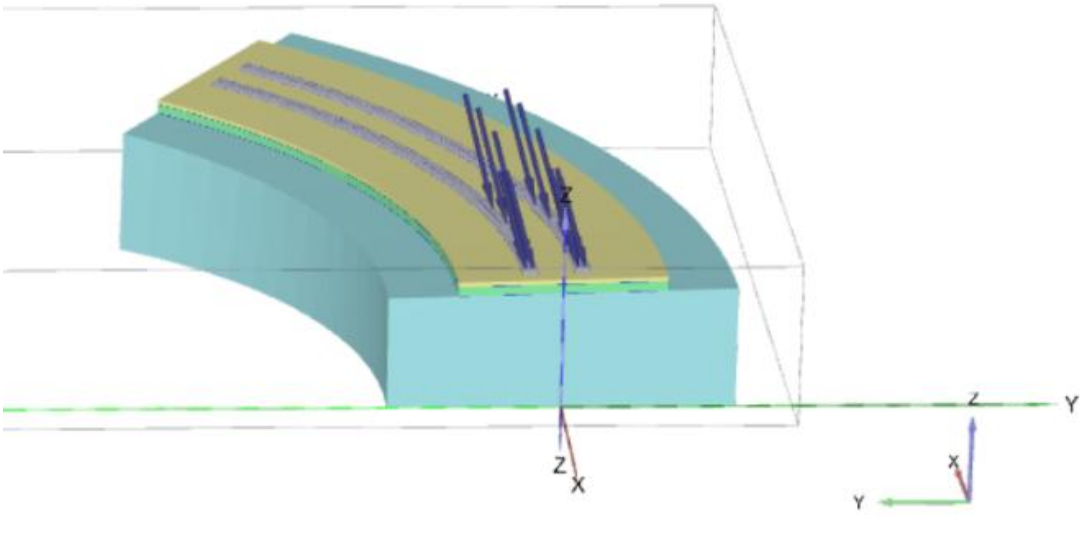

Figure 4.7: Vehicle at phase 3

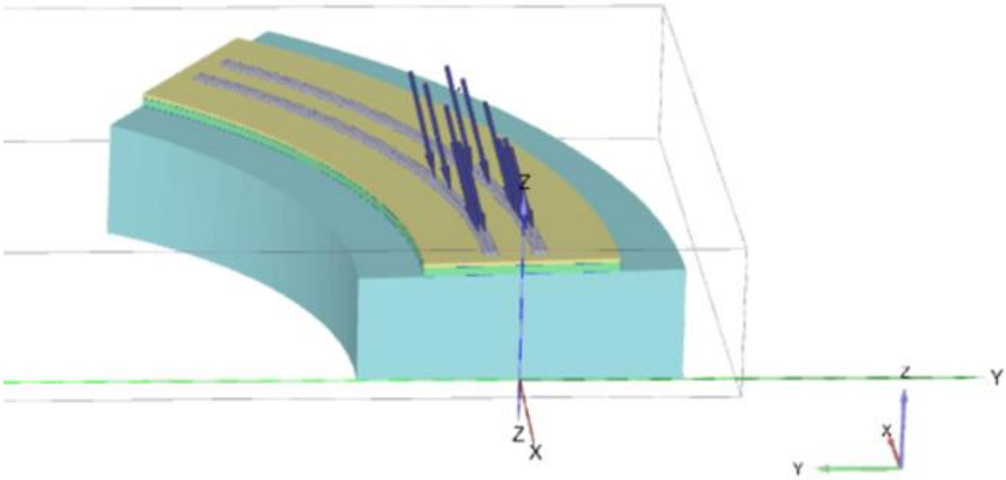

Figure 4.8: Vehicle at phase 14

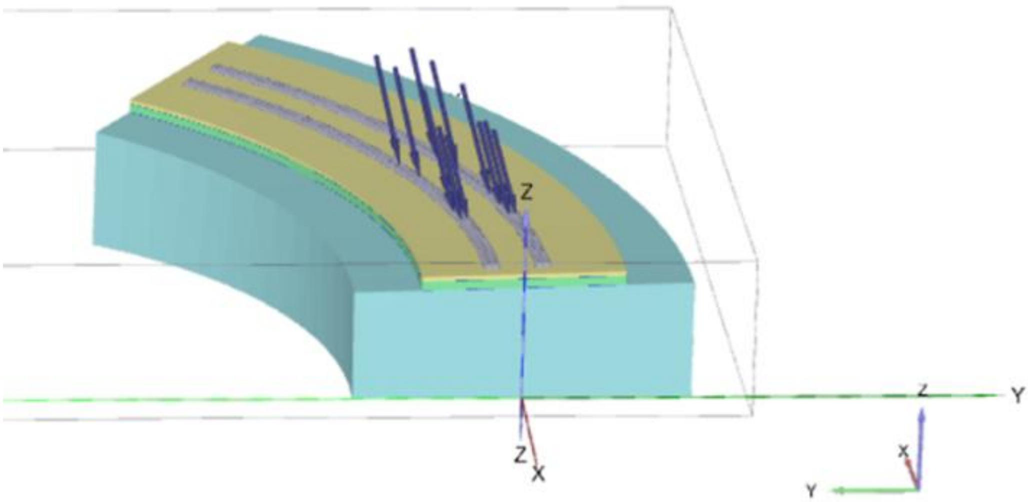

Figure 4.9: Vehicle at phase 28

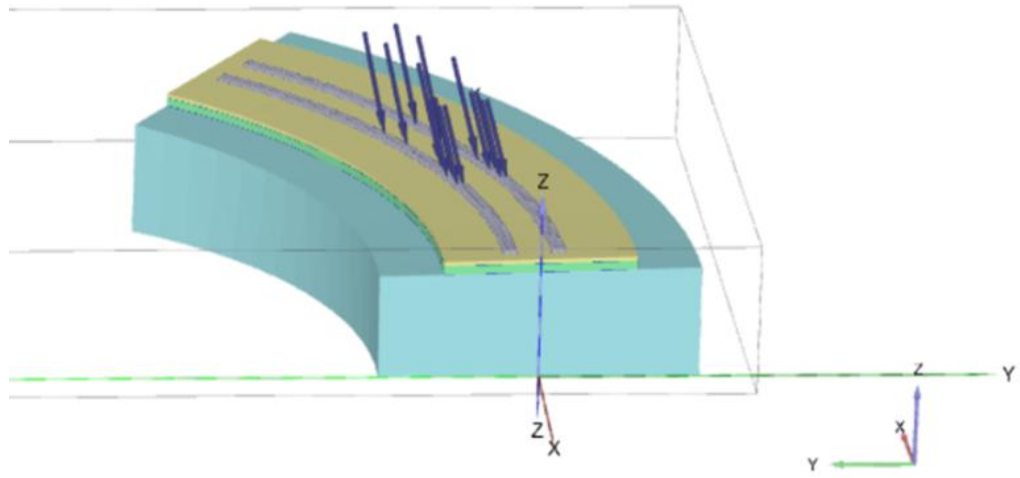

Figure 4.10: Vehicle at phase 42

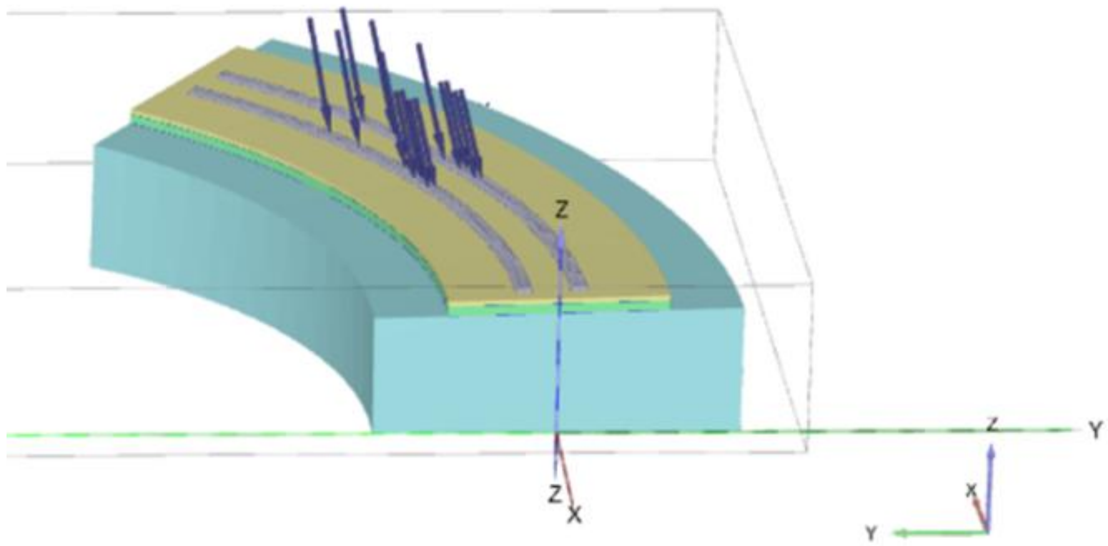

Figure 4.11: Vehicle at phase 56

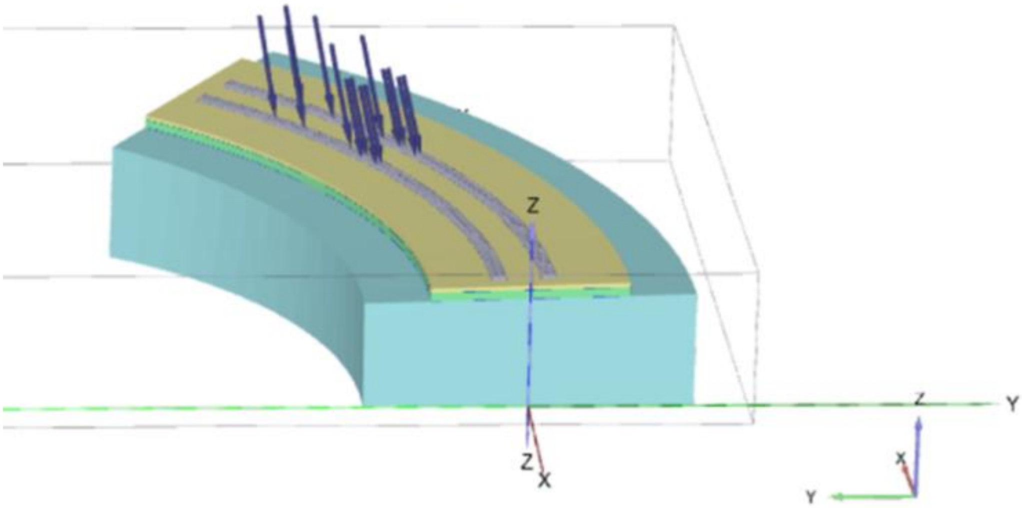

Figure 4.12: Vehicle at phase 70

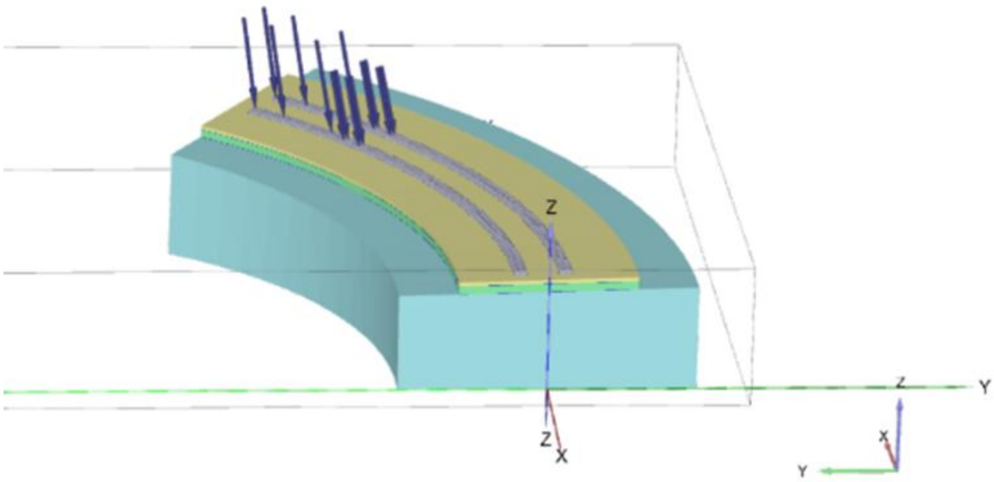

Figure 4.13: Vehicle at phase 88

4.5.1 Automation for pre and post processing

Four tyre paths trace concentric circular arcs on the curved pavement surface. Coordinates (x, y, z) of all point loads were computed using circular geometry equations and fully automated using Python eliminating manual computation across the 88 loading phases. Centrifugal force, $F_c = \frac{Mv^2}{R}$ and tangential force $F_t = M \cdot a$) by Wowk (2015) were computed for each phase using an initial speed of 9.5 m/s and acceleration of 0.5 m/s^2 and resolved into global Cartesian components F_x and F_y for each loading phase on each tyre point load on each radial path different for different phases and assigned accordingly using automation. All response parameters were extracted at a fixed reference point corresponding to the location of the second last tire of the second concentric tire path (critical) in each phase applied consistently across all simulations using automation. The python interface was used for both preprocessing and post processing.

The process used in python scripting are:

- Geometry creation from the obtained data.
- From python script, creation of the whole point loads setup through input command:
  "s_i, g_i = new_server('localhost', PORT, password=PASSWORD) and g_i.gotostages() Brinkgreve (2019). "
- Creation of 88 phases, activating particular 14-point loads in each phase.
- By providing coordinates of every point load, the equations of force, and the respective velocity according to the location of the point load, assigned a corresponding F_x, F_y and F_z.
- After the full preprocessing, the model was run.
- When the run was complete, the required data was extracted using the output python script with output command:
  "s_o, g_o = new_server('localhost', PORT, password=PASSWORD) Brinkgreve (2019)."

The parameters extracted to evaluate are listed below in table:

Table 4.6: Extracted pavement response parameters

Parameter	Symbol	Location	Significance
Tensile strain	ε_{long}	Base of Asphalt	IRC 37 critical fatigue strain for curved section
Vertical compressive strain	ε_{zz}	Top of Subgrade	IRC 37 critical rutting strain

4.6 Geogrid Reinforcement Analysis and Comparison

Three geogrid placement configurations were evaluated against an unreinforced control which are Configuration BA (asphalt base interface only), Configuration SB (base subgrade interface only), and Configuration SB+BA (both interfaces simultaneously). For each configuration, three axial stiffness values were tested which are 300, 600, and 800 kN/m. The complete simulation matrix is presented in Table 4.7. Figure 4.14 shows the geogrids and interfaces activated for the calculation. The output was focused on the fixed reference point. Results from all phases were extracted and arranged. For the comparison, the critical strain of without geogrid was taken and strains from others were corresponding to it.

Table 4.7: Complete simulation matrix: models for pipalamod lower

Model ID	Geogrid Location	Stiffness EA (kN/m)
W0 (Control)	None-unreinforced pavement	—
BA-300	Asphalt-Base Interface	300
BA-600	Asphalt-Base Interface	600
BA-800	Asphalt-Base Interface	800
SB-300	Base-Subgrade Interface	300
SB-600	Base-Subgrade Interface	600
SB-800	Base-Subgrade Interface	800
SB+BA-300	Both Interfaces	300
SB+BA-600	Both Interfaces	600
SB+BA-800	Both Interfaces	800

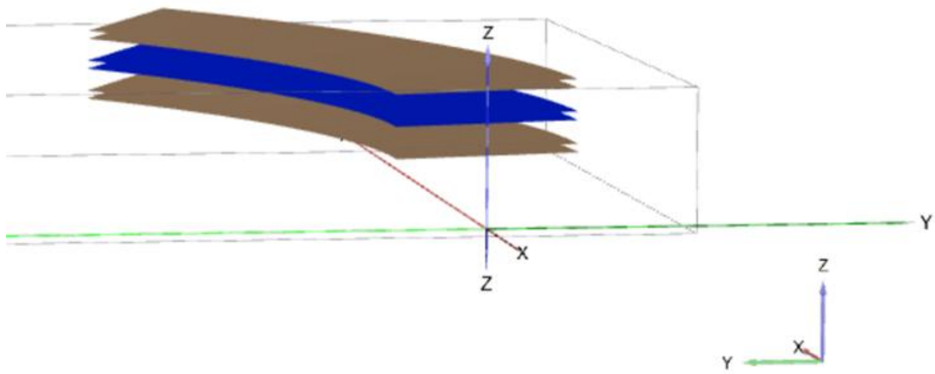

Figure 4.14: Geogrids and interfaces

In Figure 3.1, the blue surface represents the geogrid element and brown one represents interfaces. The interfaces were provided at the positive and negative side of the geogrid which were later activated in the staged construction for all phases.

5 RESULTS AND DISCUSSION

This chapter presents the simulations results which are for the unreinforced control model and other geogrid reinforced models for the Pipalamod Lower site (R = 32 m, CBR = 5.86 %, 145 MSAL). Results are presented in parts: (i) PLAXIS 3D contour visualizations providing visualization of geogrid effects; (ii) parametric comparison with fatigue and rutting life predictions. The critical phase comparison method is used throughout. The following figures present the PLAXIS 3D output contour plots for all critical response parameters shown at representative positions of curve traversal for both the No Geogrid (unreinforced) and with geogrid (reinforced) at EA = 300 kN/m models at Pipalamod Lower. These visualizations provide direct graphical evidence of how geogrid reinforcement redistributes strains throughout the curved pavement structure under the moving vehicle loading. The other geogrid also follows the similar pattern.

5.1 Tensile Strain (ε_{long}) at Base of Asphalt: No Geogrid vs Others

Comparison of ε_{long} contour distribution at the asphalt layer's bottom for the unreinforced and other different reinforced model for a particular same phase are shown from Figure 5.1 to Figure 5.4. The high-strain zone (warmer colors in the No-Geogrid plots) is visibly diminished and more diffused in the reinforced model (BA and BA+SB). The contour figures shown below are particularly of the geogrid stiffness 300 kN/m. Other geogrid stiffness follows the same patterns.

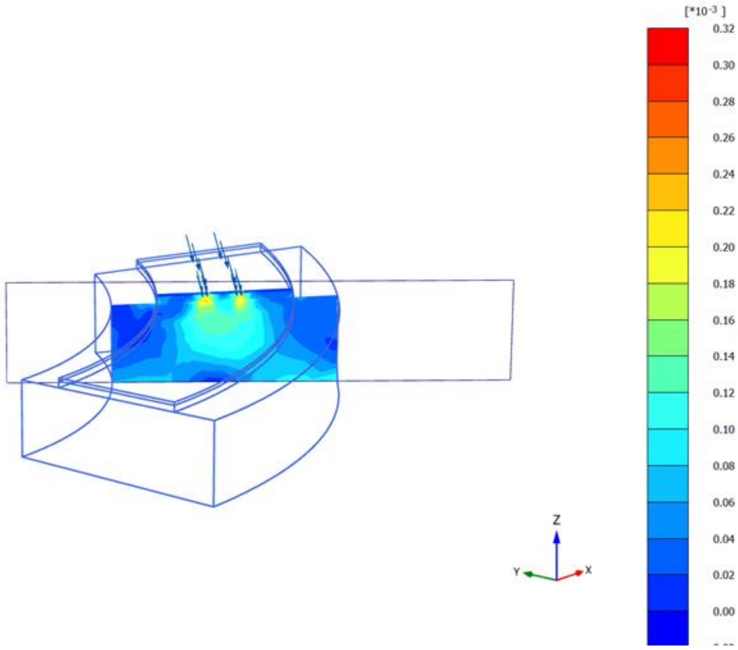

Figure 5.1: $\varepsilon_{\text{long}}$ *without geogrid*

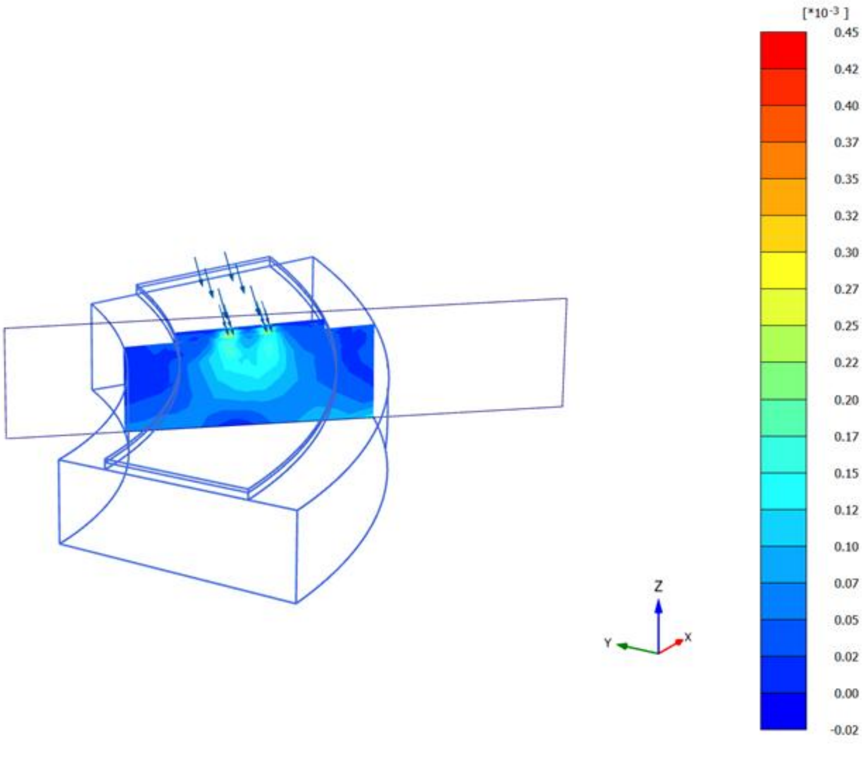

Figure 5.2: $\varepsilon_{\text{long}}$ *with SB configuration*

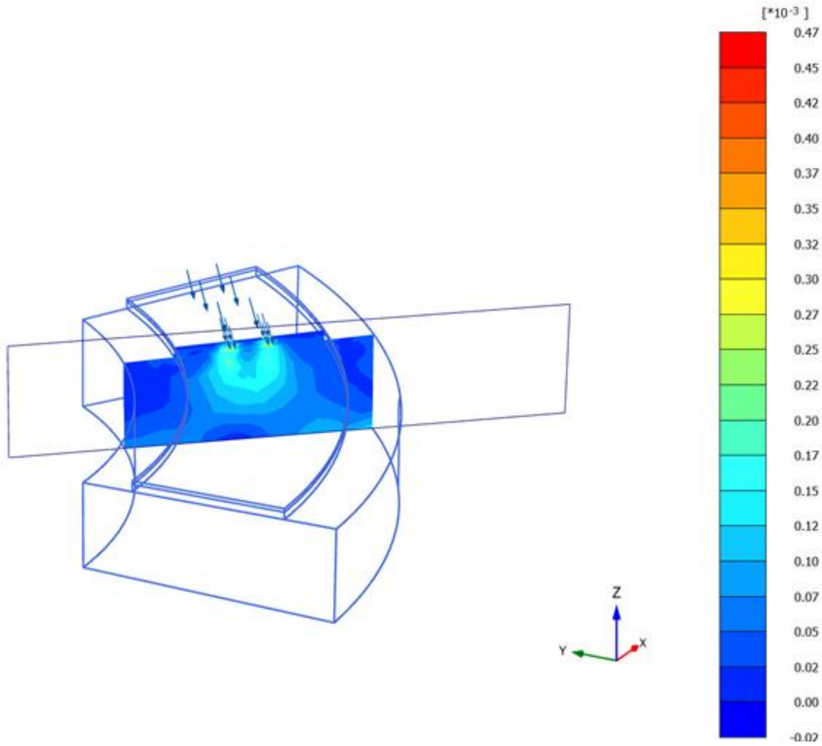

Figure 5.3: $\varepsilon_{\text{long}}$ *with BA+SB configuration*

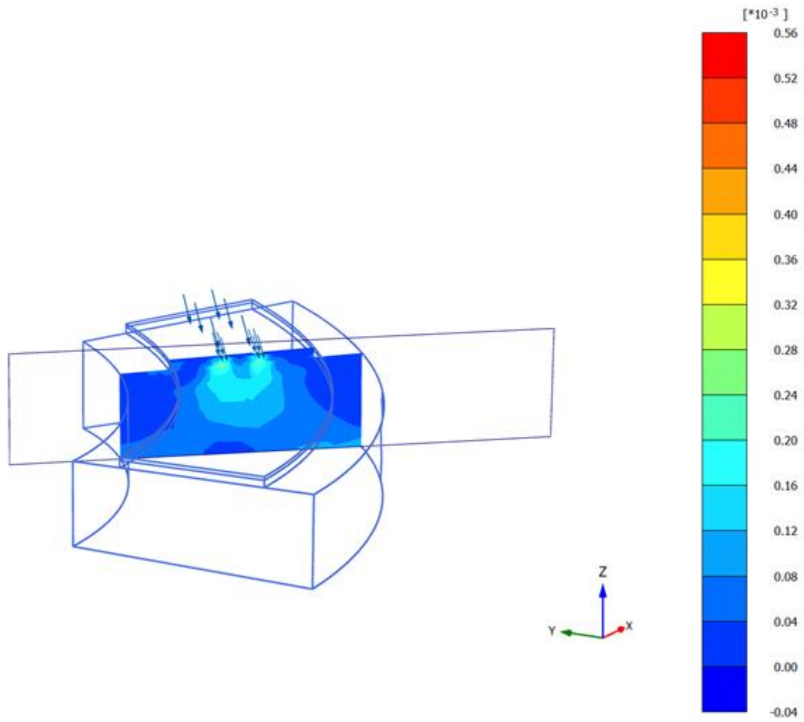

Figure 5.4: $\varepsilon_{\text{long}}$ *with BA configuration*

5.2 Compressive Strain (ε_{zz}) at Top of Subgrade: No Geogrid vs Others

The following figures Figure 5.5 to Figure 5.8 shows how the geogrid reinforcement at different configurations significantly diffuse the strain ε_{zz}. BA+SB shows the best result among other configurations. Same pattern is followed by other geogrid stiffness. The contour plots show that the use of the geogrid is beneficial in the reduction of the strains.

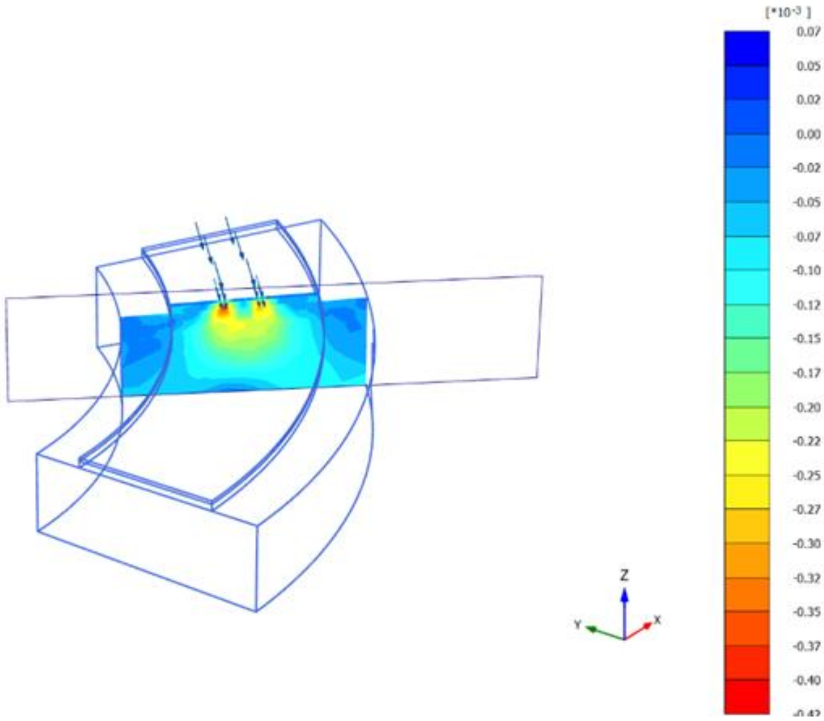

Figure 5.5: ε_{zz} without geogrid

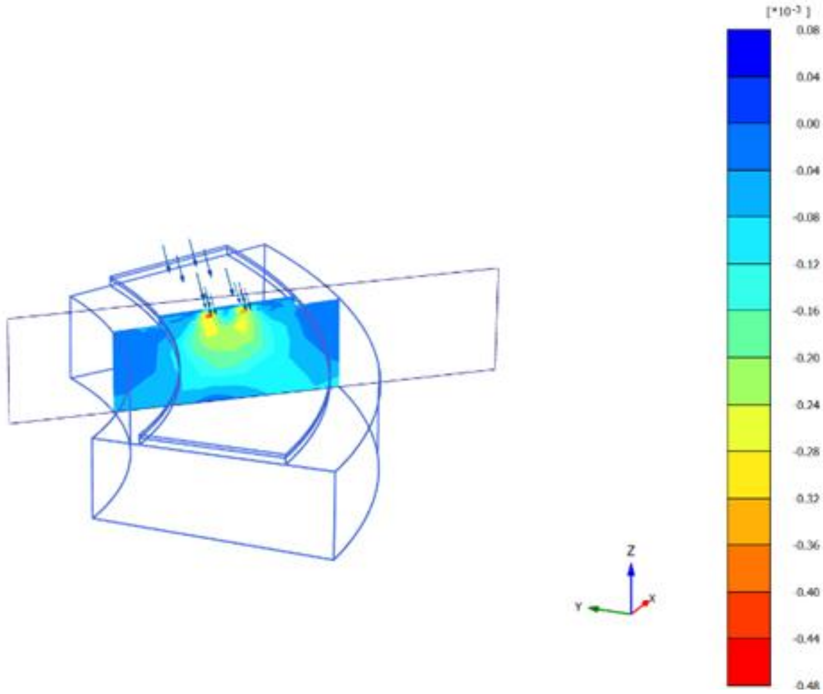

Figure 5.6: ε_{zz} with SB configuration

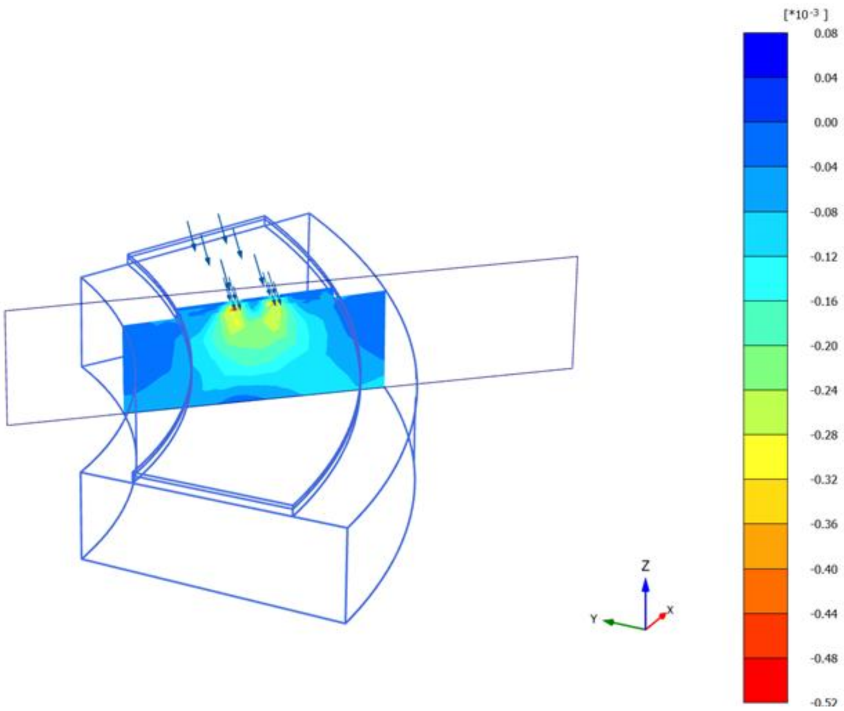

Figure 5.7: ε_{zz} with BA+SB configuration

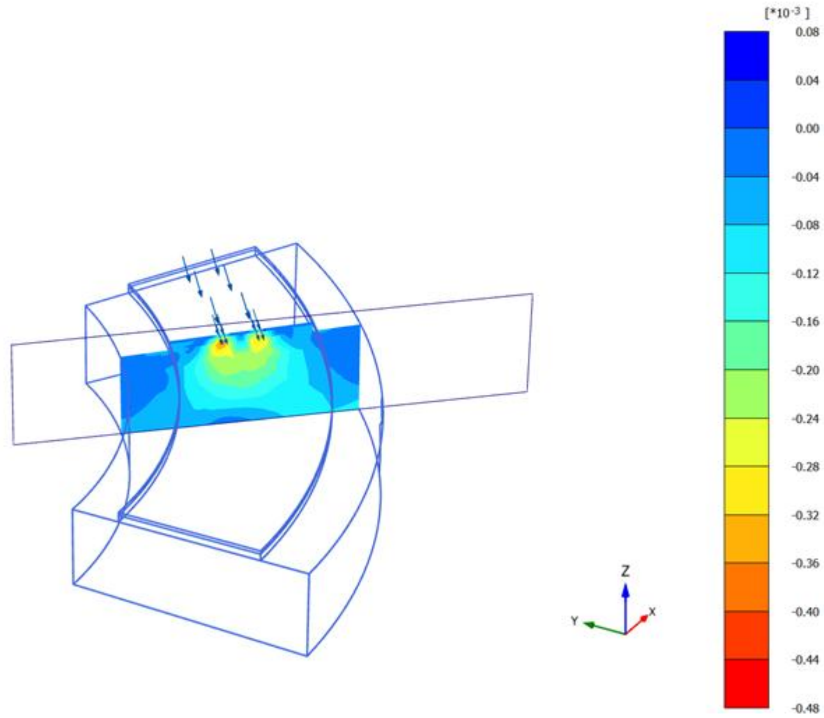

Figure 5.8: ε_{zz} with BA configuration

5.3 ε_{long} and ε_{zz} Contour Visualizations of the Model

Figure 5.9 to Figure 5.12 show the contour plots for the parameter ε_{long} at the bottom of the asphalt for the visualizations of effects on the horizontal cross section at different geogrid configurations. Similarly, Figure 5.13 to Figure 5.16 show the contour of ε_{zz} at the top of the subgrade in horizontal cross section for the visualizations of geogrid effects at different configurations.

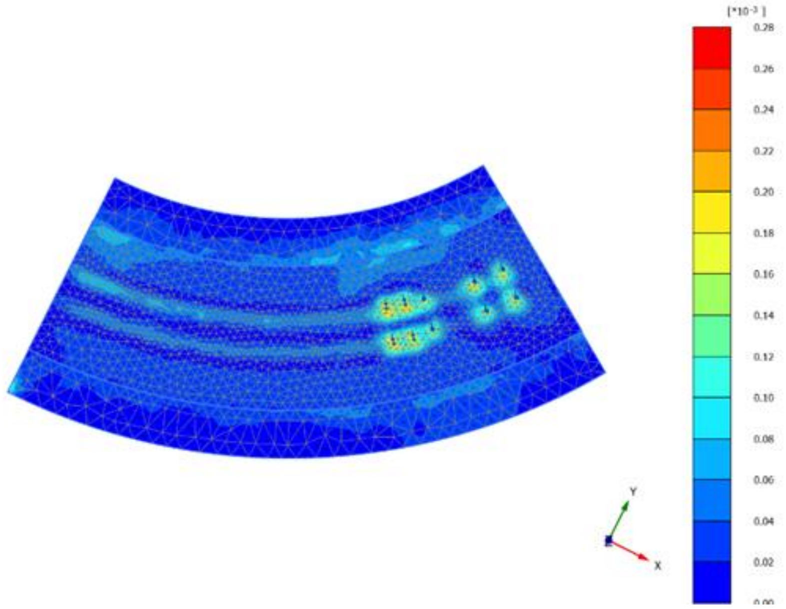

Figure 5.9: $\varepsilon_{\text{long}}$ *at bottom of asphalt without geogrid*

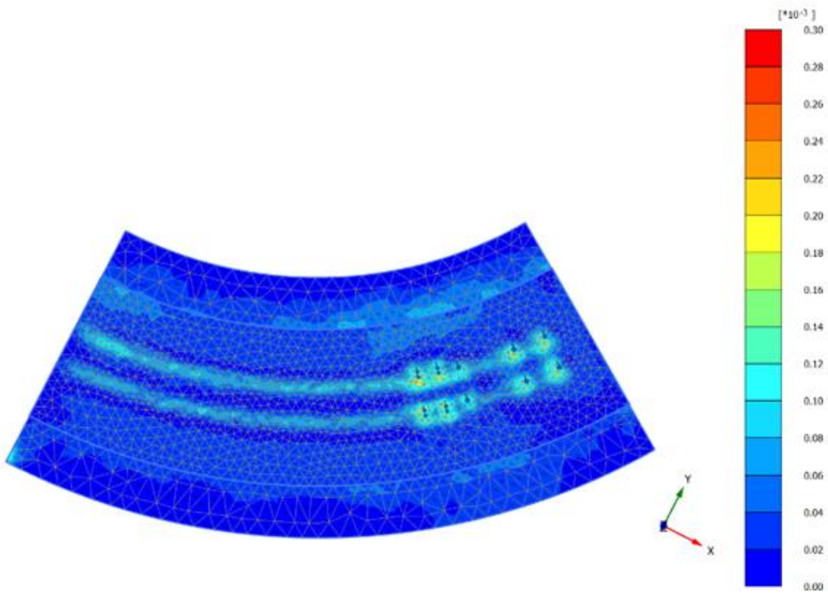

Figure 5.10: $\varepsilon_{\text{long}}$ *at bottom of asphalt of BA*

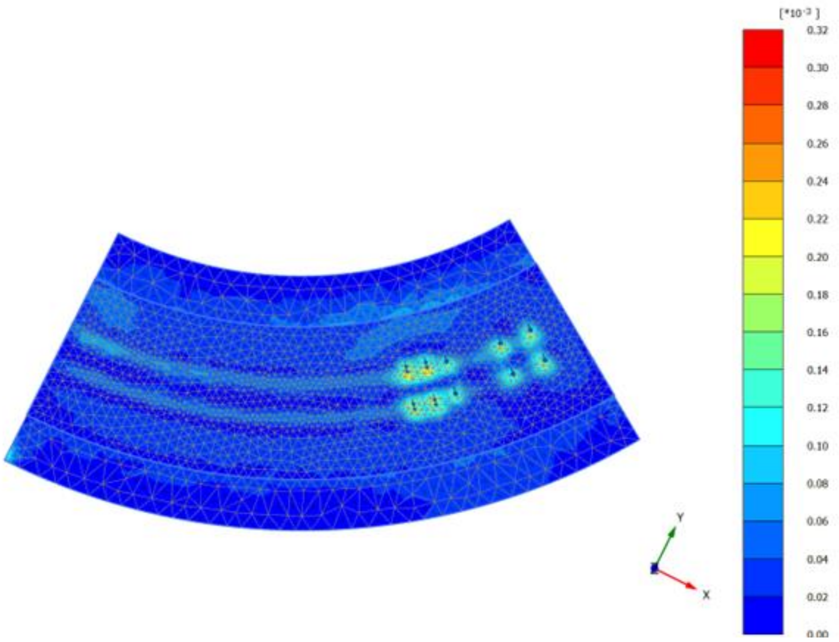

Figure 5.11: $\varepsilon_{\text{long}}$ *at bottom of asphalt of SB*

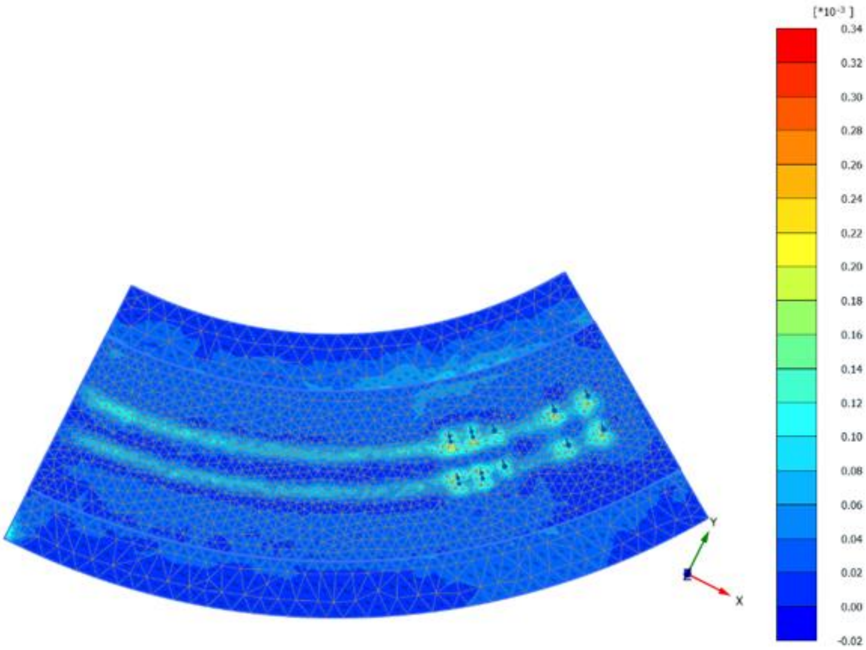

Figure 5.12: $\varepsilon_{\text{long}}$ *at bottom of asphalt of BA+SB*

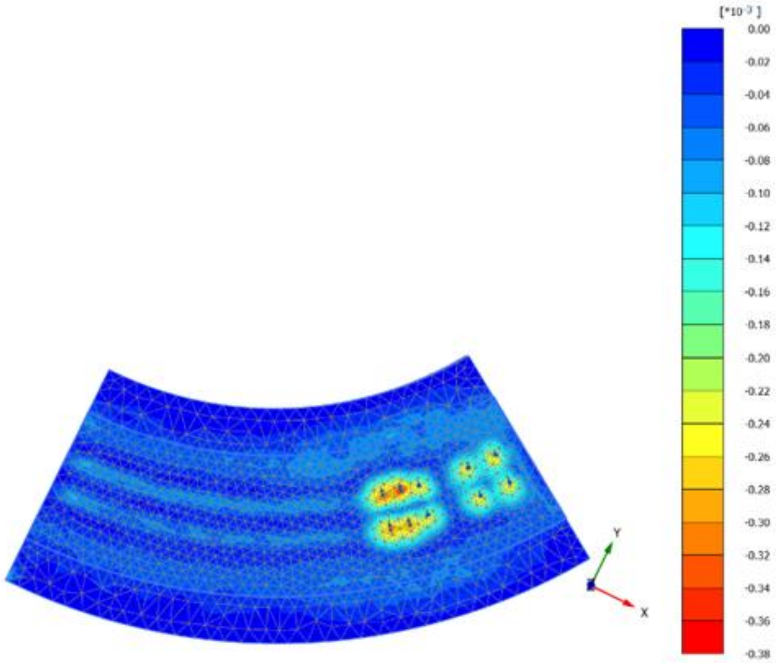

Figure 5.13: ε_{zz} at top of subgrade without geogrid

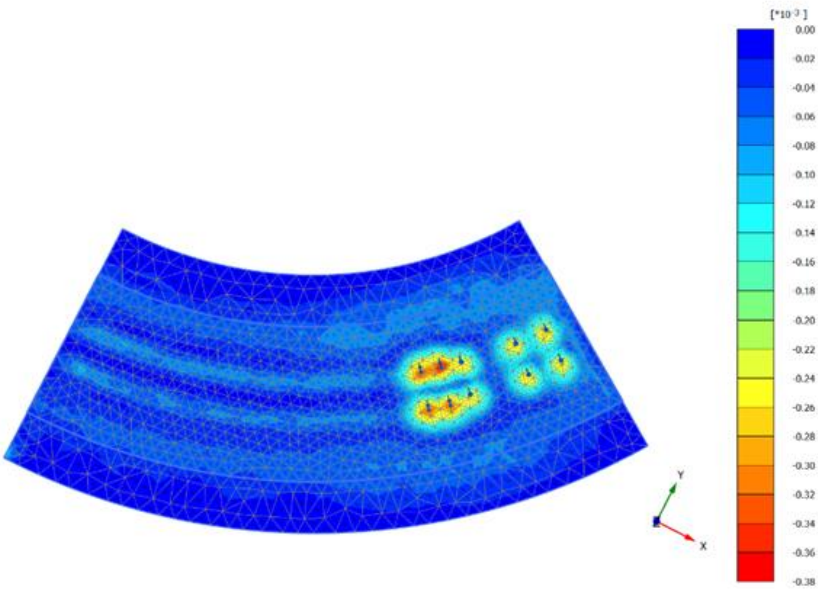

Figure 5.14: ε_{zz} at top of subgrade of BA

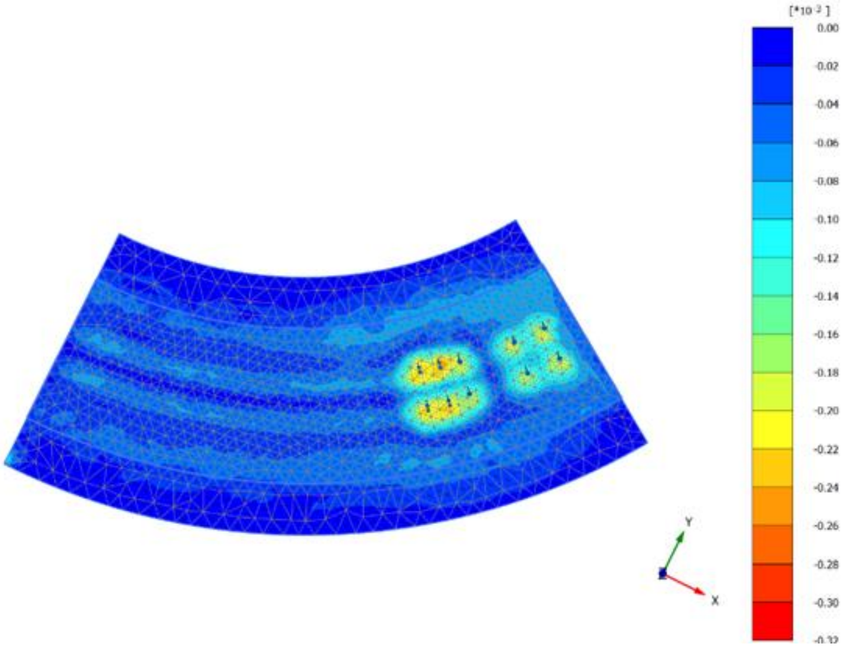

Figure 5.15: ε_{zz} at top of subgrade of SB

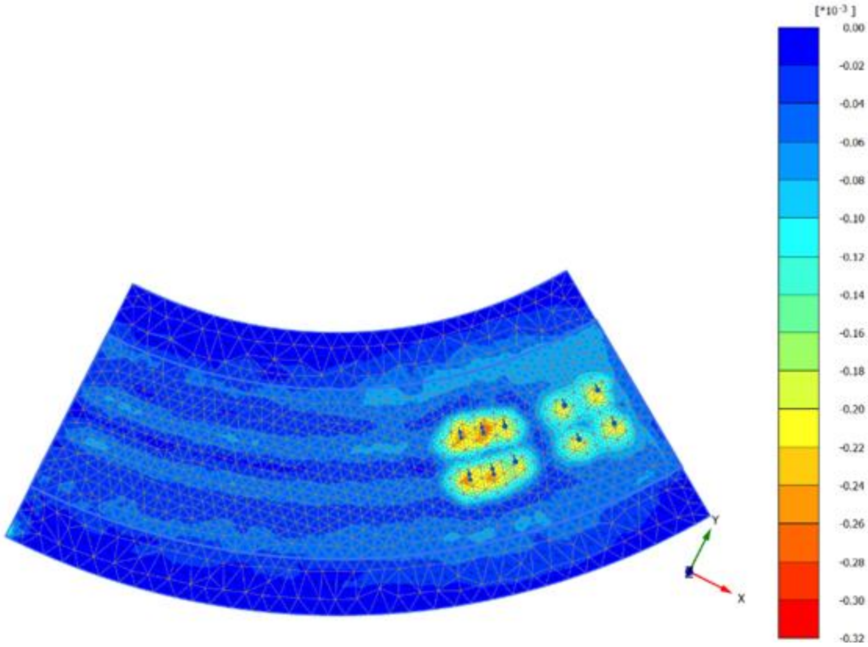

Figure 5.16: ε_{zz} at top of subgrade of BA+SB

5.4 Parametric Comparison of Geometric Configuration and Stiffness

The coming sections present an absolute values data table, strain ratio table, percentage change of strains and interpretation on obtained data for all parameters.

5.4.1 ε_{long} at *BoA: tensile strain at base of asphalt*

Table 5.1 gives ε_{long} for the respective stiffness and configuration and it shows that for single layer, BA is best rather than SB configuration.

Table 5.1: Absolute values of $\varepsilon_{\text{long}}$ *for 105 kN*

Stiffness	BA	BA+SB	SB	w_{0_G} (ref)
300	0.000189367	0.0001621	0.000202008	0.000205018
600	0.000179206	0.0001571	0.000200408	0.000205018
800	0.000172099	0.000152	0.000197001	0.000205018

Table 5.2: ε_{long} *corresponding to 80 kN*

Stiffness	BA	BA+SB	SB	w_{0_G} (ref)
300	0.00014428	0.000123505	0.000153911	0.000156205
600	0.000136538	0.000119696	0.000152692	0.000156205
800	0.000131123	0.00011581	0.000150096	0.000156205

Table 5.2 gives the visualization of $\varepsilon_{\text{long}}$ for the 80 kN after conversion. It is obtained after applying the conversion factor.

Table 5.3: Strain ratio table for $\varepsilon_{\text{long}}$

Stiffness	BA	BA+SB	SB	w_{0_G} (ref)
300	1.08	1.26	1.01	1
600	1.14	1.30	1.02	1
800	1.19	1.35	1.04	1

Table 5.3 shows the strain ratio value for each configuration and stiffness for ε_{long}. Strain ratio is calculated with the ratio of strain of without geogrid configuration to strain of particular geogrid configuration. It can be seen that the use of geogrid is beneficial as it increases the SLR.

Table 5.4: percentage change of strain ε_{long}

Stiffness	BA	BA+SB	SB	w_{0_G} (ref)
300	7.6%	20.9%	1.5%	-
600	12.6%	23.4%	2.2%	-
800	16.1%	25.9%	3.9%	-

Table 5.4 gives the value for the percentage change of ε_{long} for different configuration with respect to without geogrid value. Analysis and interpretation are as below:

- BA+SB configurations reduce tensile strain at the base of asphalt relative to the unreinforced case significantly.
- BA+SB achieves the greatest reduction of 25.86% at stiffness 800 kN/m.
- BA provides 7.63-16.05% improvement with an upward trend as stiffness increases.
- The ranking across all three BoA strain metrics (BA+SB > BA > SB) confirms that dual interface placement is the best strategy for asphalt fatigue strain reduction at Pipalamod lower site.
- But in comparison to SB, BA is the best configuration for the fatigue criteria.

5.4.2 ε_{zz} at ToS: vertical compressive strain at top of subgrade

Table 5.5 gives ε_{zz} for the respective stiffness and configuration in respect of 105kN.

Table 5.5: Absolute values of ε_{zz} for 105 kN

Stiffness	BA	BA+SB	SB	w_{0_G} (ref)
300	0.000389149	0.000327016	0.000376601	0.000394529
600	0.00038406	0.000318002	0.00036073	0.000394529
800	0.000378	0.000311002	0.000352153	0.000394529

Table 5.6: ε_{zz} strain table corresponding to 80 kN

Stiffness	BA	BA+SB	SB	w_{0_G} (ref)
300	0.000296494	0.000249155	0.000286934	0.000300593
600	0.000292617	0.000242287	0.000274842	0.000300593
800	0.000288	0.000236954	0.000268307	0.000300593

Table 5.6 gives the ε_{zz} strain table corresponding to 80 kN after applying the conversion factor. The conversion factor is linear.

Table 5.7: Strain ratio for ε_{zz}

Stiffness	**BA**	**BA+SB**	**SB**	**w_{0_G} (ref)**
300	1.01	1.21	1.05	1
600	1.03	1.24	1.09	1
800	1.04	1.27	1.12	1

Table 5.7 gives the value for the strain ratio of ε_{zz} of without geogrid to different configurations of the geogrid. It can be seen that the use of geogrid is beneficial as it increases the SLR.

Table 5.8: percentage change of ε_{zz}

Stiffness	**BA**	**BA+SB**	**SB**	**w_{0_G} (ref)**
300	1.4%	17.1%	4.5%	-
600	2.7%	19.4%	8.6%	-
800	4.2%	21.2%	10.7%	-

Table 5.8 gives the value of the percentage change of ε_{zz} of different configurations with respect to without geogrid.

Analysis and interpretation

- SB is achieves 4.54 % reduction in vertical compressive strain at the subgrade surface at stiffness 300 kN/m improving further to 10.74 % at stiffness 800kN/m.
- BA+SB reduces ε_{zz} ToS by 17.11 % at stiffness 300 by improving to 21.17% at stiffness 800 making it the best configurations for improving the rutting life too.
- But in comparison to BA, SB is the best configuration for the rutting criteria.

5.5 Effect of Geogrid Stiffness

The Table 5.9 quantifies the change in strain values from the stiffness 300 to stiffness 800 kN/m for each configuration.

Table 5.9: Comparison of strain of different stiffness

Metric	BA (300→1200)	BA+SB (300→1200)	SB (300→1200)
Elong at BoA change	2.53E-05	1.50E-05	8.01E-06
Ezz at ToS change	1.33E-05	2.10E-05	3.16E-05

It can be said that increasing the geogrid stiffness also increases the strain reduction which may not be in the significant way but is considerable.

5.6 Fatigue and Rutting Life Results

The Table 5.10 and Table 5.11 present the computed fatigue life (based on ε_{long} at BoA) and rutting life (based on ε_{zz} at ToS) for all three geogrid configurations at all three stiffness levels using equation 3 and equation 4 respectively by Congress (2018).

$$N_f = 0.5161 * C * 10^{-4} * \left[\frac{1}{\varepsilon_t}\right]^{3.89} * \left[\frac{1}{M_{Rm}}\right]^{0.854} \quad (3)$$

$$N_r = 1.4100 * 10^{-8} * \left[\frac{1}{\varepsilon_v}\right]^{4.5337} \quad (4)$$

"Equation (3)" and "Equation (4)" are from Indian Roads Congress (2018). These equations are for standard 80kN axle load.

Since all strain parameters are obtained for the 105 kN axle load, they must be converted to the corresponding 80 kN strain parameters.

Equivalent conversion factor for 105 $kN = \left(\frac{80}{105}\right) = 0.762$

Sample calculation:

For fatigue life: with Elong = 0.000205018 for 105 kN so for 80 kN = 0.000205018 *0.762= 0.000156205

$$N_f = 0.5161 * C * 10^{-4} * \left[\frac{1}{\varepsilon_t}\right]^{3.89} * \left[\frac{1}{M_{Rm}}\right]^{0.854} \quad (3)$$

"Equation (3)" is from Congress (2018).

N_f = 111.7 MSAL load

Similarly,

For rutting with ε_{zz} = 0.000394529 for 105 kN so for 80 kN = 0.000300593

$$N_r = 1.4100 * 10^{-8} * \left[\frac{1}{\varepsilon_v}\right]^{4.5337} \quad (4)$$

"Equation (4)" is from Congress (2018).

Nr = 130.9 MSAL load

So, the following table follows the same calculation as above.

5.6.1 Fatigue life results: ε_{long} at BoA basis

Table 5.10 gives the fatigue life of the different configurations and stiffness of the geogrid. The effectiveness of geogrid can be seen clearly. Figure 5.17 shows that the fatigue life increases when stiffness of the geogrid is increased. BA+SB shows the better performance.

Table 5.10: Fatigue life (MSAL) by geogrid configuration and stiffness

Stiffness	**BA**	**BA+SB**	**SB**	**w_{0_G} (ref)**
300	152.2	278.6	118.3	111.7
600	188.6	314.7	122.1	111.7
800	220.7	357.8	130.5	111.7

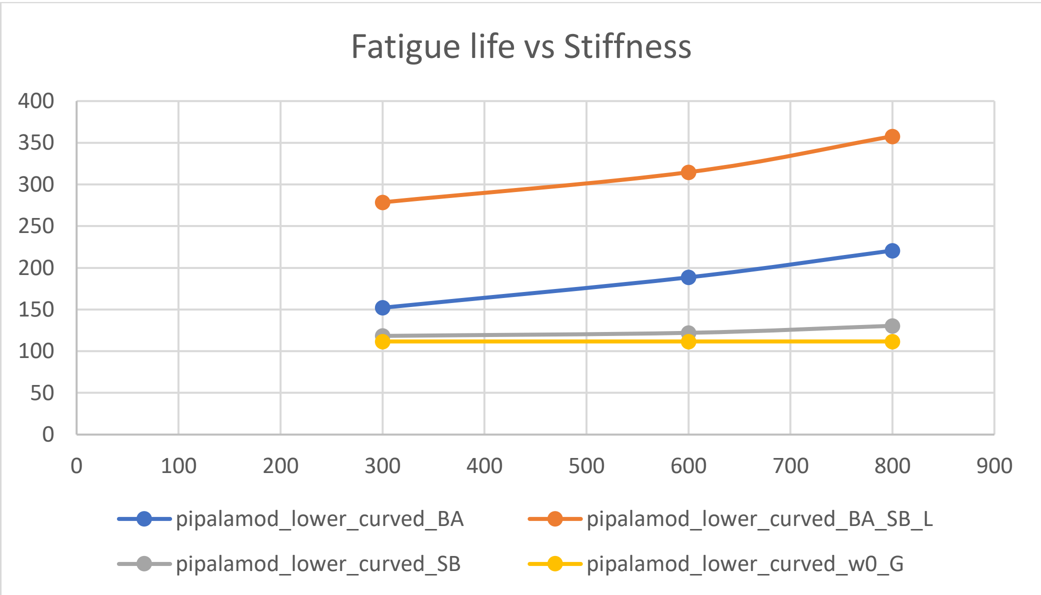

Figure 5.17: Fatigue life results

5.6.2 *Rutting life results: ε_{zz} at ToS basis*

Table 5.11: Rutting life (MSAL) by geogrid configuration and stiffness

Stiffness	BA	BA+SB	SB	w_{0_G} (ref)
300	139.3	306.6	161.6	130.9
600	147.9	348.1	196.4	130.9
800	158.9	384.9	219.1	130.9

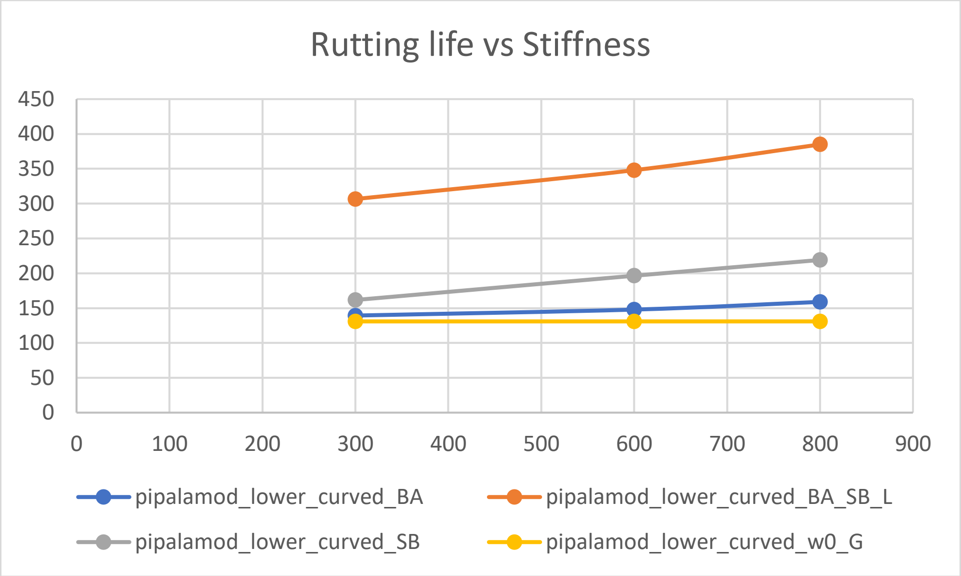

Figure 5.18: Rutting life vs stiffness

Table 5.11 gives the rutting life for the different stiffness and the configurations of the geogrid. SB and BA+SB achieve higher rutting lives. Figure 5.18 help to visualize that increasing the stiffness increases rutting life.

5.6.3 *Calculation of the service life ratio (SLR)*

The road section is designed for the MSAL of 145 MSAL. So, this study compares the obtained rutting and fatigue life with the 145 MSAL to get the Service Life Ratio (SLR).

Sample calculation:

For BA at stiffness 300 kN/m,

$$Service\ Life\ Ratio\ (SLR) = \frac{152.1}{145} = 1.04$$

Table 5.12: Service life ratio based on the fatigue life.

Stiffness	BA	BA+SB	SB	w_{0_G} (ref)
300	1.1	1.9	0.8	0.8
600	1.3	2.2	0.8	0.8
800	1.5	2.5	0.9	0.8

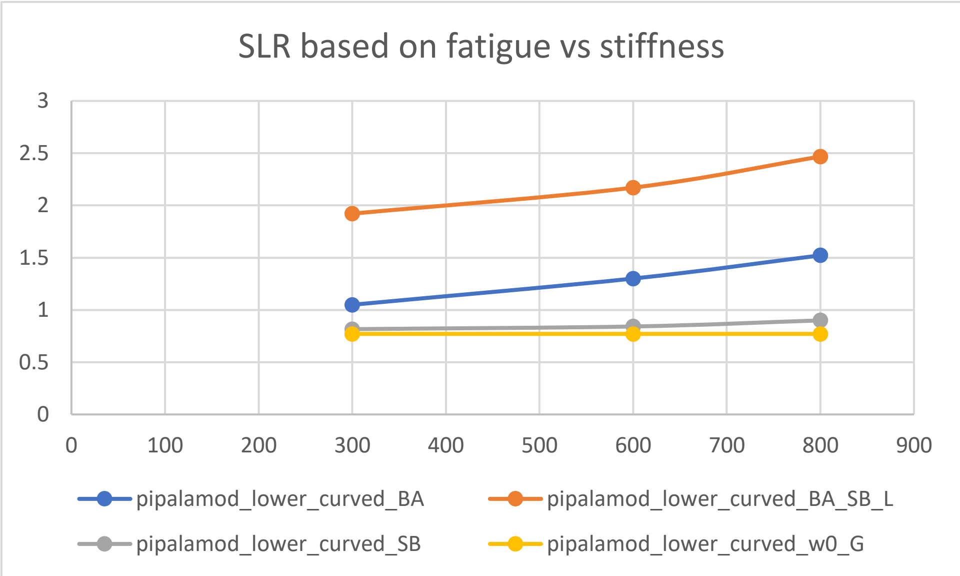

Figure 5.19: SLR based on fatigue life

The Table 5.12 gives the service life ratio for the different configuration and stiffness based on the fatigue life which clearly shows the benefits of geogrid. In Figure 5.19, it can be seen that if the stiffness increases, SLR based on fatigue life increases. Interpretation for fatigue life are:

- Initially, the road is designed from IITPAVE. It takes standard 80 kN axle load. It doesn't consider effects of curvature, tangential force, centrifugal force and longitudinal gradient. There is no provision to employ theses parameters in IITPAVE software. Also, it models all the layers as a linear elastic.
- So, from above data, it can be said that the designed value becomes insufficient if we consider the curvature and gradient effects as said above. That means, if the above effects are considered, the road will be sufficient for only 0.770*145=111.7 MSAL if no geogrid is used, which fails to meet the designed cumulative load of 145 MSAL.
- To meet the 145 MSAL design cumulative load, the geogrids must be used on the interfaces of the layers in the curved sections of the road. For fatigue, BA and BA+SB configuration meet the expectation.

SB increases the load capacity compared to no geogrid but doesn't meet the designed cumulative load which is 145 MSAL.

- SB+BA achieves higher SLR compared to another configuration.

Similarly, for the rutting life

Table 5.13: Service life ratio based on the rutting life

Stiffness	BA	BA+SB	SB	w_{0_G} (ref)
300	0.9	2.1	1.1	0.9
600	1.1	2.4	1.4	0.9
800	1.1	2.7	1.5	0.9

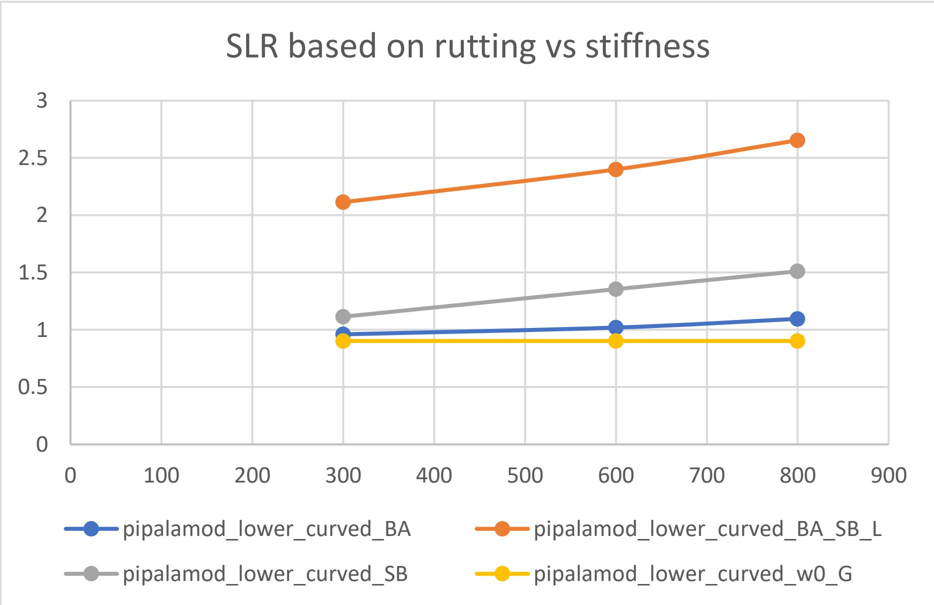

Figure 5.20: SLR based on rutting

The Table 5.13 provides SLR based on the rutting life for different configurations and stiffness of the geogrids which clearly shows that SLR is improved when the geogrid is used. Figure 5.20 shows that increasing stiffness increases the SLR based on rutting life. Interpretation for rutting life are:

- The interpretation of above SLR for the rutting is similar to the fatigue. Without geogrid, it fails to meet the designed load of 145 MSAL. That is, if no geogrid is used in curved sections, it gives only up to $0.90 * 145 = 130.96\ MSAL$ which is lower than designed one.
- So, for the rutting life to meet the designed load, geogrid must be used to compensate the effects of the curvature and the vehicle configuration. For

this, SB and BA+SB meet the expectation. BA has more SLR compared to no-geogrid configuration but fails to meet the expectation.

- SB+BA achieves higher SLR compared to another configuration.

6 CONCLUSIONS AND RECOMMENDATIONS

It is found that both the geogrid configuration and the stiffness have effect on the fatigue and rutting life of the flexible pavement.

6.1 Conclusions

The focus of this study is to analyze the performance of the geogrids on the curved sections of the road with longitudinal gradient. From the study, it can be said that the design for the straight road sections totally underestimate the effects of curvature, longitudinal gradient and heavy vehicle configuration in the curved road alignment.

The following conclusions are drawn from the parametric analysis of four geogrid placement configurations and three stiffness levels:

- Geogrid placement position is the dominant variable in pavement structural response compared to the stiffness level.
- BA+SB achieves the largest reductions in all strain components and has strong subgrade and asphalt fatigue protection making it the best configuration when both failure modes are considered simultaneously.
- No single geogrid placement simultaneously optimizes both response parameters. The design engineer must identify the governing failure mode and select placement accordingly.
- Fatigue life: BA+SB placement extends fatigue life much more relative to no-geogrid. BA comes to the second position compared to BA+SB. So, for this site, BA+SB is better for fatigue life and for Rutting life: BA+SB placement extends rutting life relative to no-geogrid significantly. SB also extends it in the same way. BA comes to the third position.
- For the heavy axle vehicle loading, the rutting life must be greater than the fatigue life, which is satisfied in this thesis study.
- Base-Asphalt (BA) placement primarily controls fatigue while Subgrade-Base (SB) placement is more effective for rutting.
- The design load adopted for the straight road sections is not sufficient for heavy vehicle moving in horizontal curve section with longitudinal gradient. For achieving the life both fatigue and rutting equal or more than the design life, geogrids must be incorporated in sharp curved sections of the highway considering the failure criteria.

- Single pass simulation represents the peak structural benefit of reinforcement but cumulative traffic cycles will decrease this through polymeric creep and aggregate abrasion.

6.2 Recommendations

The following recommendations can be listed from this study:

- Implement double-layer design: Use dual configuration (BA+SB) for heavy traffic sections of the Prithvi Highway, especially on very sharp curves with high longitudinal gradient.
- Prioritize BA interface: If limited to one layer on curves, prioritize the Base-Asphalt interface to mitigate fatigue failure.
- Prioritize SB interface: If limited to one layer on curves, prioritize the subgrade-base interface to mitigate rutting failure.
- Long term cyclic loading and multiple passes simulation need to be done to develop cumulative damage models and directly compute fatigue life (N_F) and rutting life (N_R) under moving loads in combined curvature gradient sections of the pavement.
- Viscoelastic asphalt modelling should be done to capture time dependent bituminous layer behavior under variable speed loading.
- Extended site coverage to other hilly road corridors in Nepal (Arniko Highway, Siddhartha Highway) are required to develop regional design charts for geogrid specification.

7 REFERENCES

Abdulhafedh, A. (2019). Design of superelevation of highway curves: An overview and distribution methods. *Journal of City and Development*, *1*(1), 35–40.

Abu-Farsakh, M. Y., Gu, J., Voyiadjis, G. Z., & Chen, Q. (2014). Mechanistic–empirical analysis of the results of finite element analysis on flexible pavement with geogrid base reinforcement. *International Journal of Pavement Engineering*, *15*(9), 786–798. https://doi.org/10.1080/10298436.2014.893315

Beer, F. P., Johnston, E. R., Mazurek, D. F., & Cornwell, P. J. (2019). *Vector Mechanics for Engineers: Statics and Dynamics* (12th ed.). McGraw-Hill.

Bennett, C. R., & Pedersen, L. (2023). Modelling Pavement Deterioration of Strategic Road Network in Nepal Based on Different Performance Indicators. *Proceedings of the 12th International Conference on Managing Pavement Assets (ICMPA)*. http://lpcb.org/index.php/document-library/pavement-deterioration/2023-nepal-modelling-pavement-deterioration-of-strategic-road-network-in-nepal-based-on-different-performance-indicators

Beskou, N. D., & Muho, E. V. (2023). Review on dynamic response of road pavements to moving vehicle loads; part 2: Flexible pavements. *Soil Dynamics and Earthquake Engineering*, *175*, 108248. https://doi.org/10.1016/j.soildyn.2023.108248

Brinkgreve, R. B. J. (2019). *PLAXIS 3D Reference Manual*. Plaxis BV / Bentley Systems.

Calvarano, L. S., Palamara, R., Leonardi, G., & Moraci, N. (2017). 3D-FEM Analysis on Geogrid Reinforced Flexible Pavement Roads. *IOP Conference Series: Earth and Environmental Science*, *95*(2). https://doi.org/10.1088/1755-1315/95/2/022024

Cardenas, J. J., & Al-Qadi, I. L. (2024). Impact of Dynamic Wheel Loading on Flexible Pavement Responses for Non-Free Rolling Conditions. *Transportation Research Record*, *2678*(11), 761–778. https://doi.org/10.1177/03611981241242378

Chhetri, S., & Deb, P. (2024). Finite Element Analysis of Geogrid-Incorporated Flexible Pavement with Soft Subgrade. *Applied Sciences*, *14*(13), 5798. https://doi.org/10.3390/app14135798

Indian Roads Congress. (2018). *IRC:37-2018 - Guidelines for the Design of Flexible Pavements* (4th Revision). Indian Roads Congress.

Correia, N. S., & Zornberg, J. G. (2018). Strain Distribution along Geogrid-Reinforced Asphalt Overlays under Traffic Loading. *Geotextiles and Geomembranes*, *46*(1), 111–120. https://doi.org/10.1016/j.geotexmem.2017.10.002

Elnashar, G., Bhat, R. B., & Sedaghati, R. (2019). Modeling and dynamic analysis of a vehicle-flexible pavement coupled system subjected to road surface excitation. *Journal of Mechanical Science and Technology*, *33*(7), 3115–3125. https://doi.org/10.1007/s12206-019-0606-5

Faheem, H., & Hassan, A. M. (2014). 2D PLAXIS Finite Element Modeling of Asphalt-Concrete Pavement Reinforced with Geogrid. *JES - Journal of Engineering Sciences, Assiut University, Faculty of Engineering*, *42*(6), 1336–1348.

Fitzpatrick, K., & Kahl, K. (1992). *A Historical and Literature Review of Horizontal Curve Design*. Texas Transportation Institute, Texas A&M University.

Giroud, J.-P., & Noiray, L. (1981). Geotextile-Reinforced Unpaved Road Design. *Journal of the Geotechnical Engineering Division, ASCE*, *107*(GT9), 1233–1254.

Gu, F., Luo, X., Luo, R., Hajj, E. Y., & Lytton, R. L. (2017). A Mechanistic-Empirical Approach to Quantify the Influence of Geogrid on the Performance of Flexible Pavement Structures. *Transportation Geotechnics*, *12*, 71–82. https://doi.org/10.1016/j.trgeo.2017.08.005

Guo, J., Yang, S., Sun, Y., Chao, Z., Yang, R., & Cheng, H. (2021). Analysis of Shear Stress and Rutting Performance of Semirigid Base Asphalt Pavement on Steep Longitudinal Slope. *Advances in Civil Engineering*, *2021*(1). https://doi.org/10.1155/2021/4445653

Haas, R., Walls, J., & Carroll, R. G. (1988). Geogrid reinforcement of granular bases in flexible pavements. *Transportation Research Record*, *1188*(1), 19–27.

Hemeda, S. (2022). Geotechnical modelling and subsurface analysis of complex underground structures using PLAXIS 3D. *International Journal of Geo-Engineering*, *13*(1), 9. https://doi.org/10.1186/s40703-022-00177-4

Himes, S. C., & Donnell, E. T. (2014). Reliability Approach to Horizontal Curve Design. *Transportation Research Record*, *2436*(1), 51–59. https://doi.org/10.3141/2436-06

Ibrahim, E. M., El-Badawy, S. M., Ibrahim, M. H., Gabr, A., & Azam, A. (2017). Effect of geogrid reinforcement on flexible pavements. *Innovative Infrastructure Solutions*, *2*(1). https://doi.org/10.1007/s41062-017-0102-7

IS 2720-1. (1983). *IS 2720-1 (1983): Methods of test for soils, Part 1: Preparation of dry soil samples for various tests*.

Kwon, J., Tutumluer, E., & Konietzky, H. (2008). Aggregate base residual stresses affecting geogrid reinforced flexible pavement response. *International Journal of Pavement Engineering*, *9*(4), 275–285. https://doi.org/10.1080/10298430701582347

Leonardi, G., & Suraci, F. (2022). A 3D-FE Model for the Rutting Prediction in Geogrid Reinforced Flexible Pavements. *Sustainability*, *14*(6), 3695. https://doi.org/10.3390/su14063695

Luo, Y., Wang, X., Jiang, A., Li, M., & Song, L. (2023). *Research on Rutting Equalization Control of Asphalt Pavement under Different Working Conditions*. https://doi.org/10.20944/preprints202308.1434.v1

Mehta, A., Mishra, A., Nikumbh, K., Ponkshe, T., & Yadav, S. (2021). Design of Flexible Pavement as per IRC:37-2018 and using IIT-Pave. *IJSRD - International Journal for Scientific Research and Development*, *9*(9). https://www.ijsrd.com/articles/IJSRDV9I90093.pdf

More, S. K., Kumbhar, S. S., & Asha, P. (2021). Effect of Water Content on Shear Strength of Black Cotton Soil. *IOP Conference Series: Earth and Environmental Science*, *822*(1), 012052. https://doi.org/10.1088/1755-1315/822/1/012052

Pandey, S., Rao, K. R., & Tiwari, D. (2012). Effect of Geogrid Reinforcement on Critical Responses of Bituminous Pavements. *Proceedings of the 25th ARRB Conference - Shaping the Future: Linking Policy, Research and Outcomes*.

Perkins, S. W. (1999). Mechanical Response of Geosynthetic-Reinforced Flexible Pavements. *Geosynthetics International*, *6*(5), 347–382. https://doi.org/10.1680/gein.6.0157

Pokharel, R., Bertolini, L., Te Brömmelstroet, M., & Acharya, S. R. (2020). Spatio-temporal evolution of cities and regional economic development in Nepal: Does transport infrastructure matter? *Journal of Transport Geography*, *90*, 102904. https://doi.org/10.1016/j.jtrangeo.2020.102904

Polisetti, S. M., & Baadiga, R. (2025). Engineering Geogrid Enabled Low Carbon and Aggregate Efficient Flexible Pavements. *Scientific Reports*, *15*, 33944. https://doi.org/10.1038/s41598-025-10066-2

Sivaprakash, G., Jayaraman, M., Bhuvaneshwari, S., & Padmarekha, A. (2025). Analysis of Geogrid Reinforced Flexible Pavement Using PLAXIS 2D. In

Ground Engineering and Applications. IYGEC 2021 (Vol. 429, pp. 399–411). Springer Singapore. https://doi.org/10.1007/978-981-96-1373-1_35

Wang, H., & Al-Qadi, I. L. (2010). Near-Surface Pavement Failure under Multiaxial Stress State in Thick Asphalt Pavement. *Transportation Research Record - Journal of the Transportation Research Board*, *2154*(1), 91–99. https://doi.org/10.3141/2154-08

Wang, H., Al-Qadi, I. L., & Stanciulescu, I. (2014). Effect of Surface Friction on Tire-Pavement Contact Stresses during Vehicle Maneuvering. *Journal of Engineering Mechanics, ASCE*, *140*(4), 04014001. https://doi.org/10.1061/(ASCE)EM.1943-7889.0000691

Webster, S. L. (1992). Geogrid Reinforced Base Courses for Flexible Pavements for Light Aircraft: Test Section Construction, BehaviorUnderTraffic, Laboratory Tests, and Design Criteria. *Technical Report GL-93-6. ASAE Waterways Experiment Station, Vicksburg, Mississippi, USA*, (May).

Wowk, V. (2015). What is Centrifugal Force? *Sound & Vibration*, 13.

Zaghloul, S., & White, T. (1993). Use of a three-dimensional, dynamic finite element program for analysis of flexible pavement. In *Transportation Research Record* (Number 1388).

Zheng, M., Han, L., Wang, C., Xu, Z., Li, H., & Ma, Q. (2017). Simulation of Permanent Deformation in High-Modulus Asphalt Pavement with Sloped and Horizontally Curved Alignment. *Applied Sciences*, *7*(4), 331. https://doi.org/10.3390/app7040331

APPENDIX A: GEOTECHNICAL LABORATORY TEST RESULTS

This annex presents the complete geotechnical laboratory test results for the Pipalamod Lower subgrade soil sample. All tests were conducted in accordance with IS 2720 series standards at the Civil Materials Testing Laboratory (CMTL), Pulchowk Campus.

A.1 Liquid Limit

S.No.	Observations and Calculations	Det. 1	Det. 2	Det. 3
	Observations			
1	Number of blows (N)	32	29	24
2	Water content can No.	S2N1	S2N2	S2N3
3	Mass of empty can (M1) (gm)	23.4	17.24	24.75
4	Mass of can + wet soil (M2) (gm)	34.41	32.06	36.86
5	Mass of can + dry soil (M3) (gm)	31.76	28.42	33.87
	Calculations			
6	Mass of water = M2 − M3 (gm)	2.65	3.64	2.99
7	Mass of dry soil = M3 − M1 (gm)	8.36	11.18	9.12
8	Water content (%)	31.699	32.558	32.785
	Result (LL for N=25)	**32.753**		

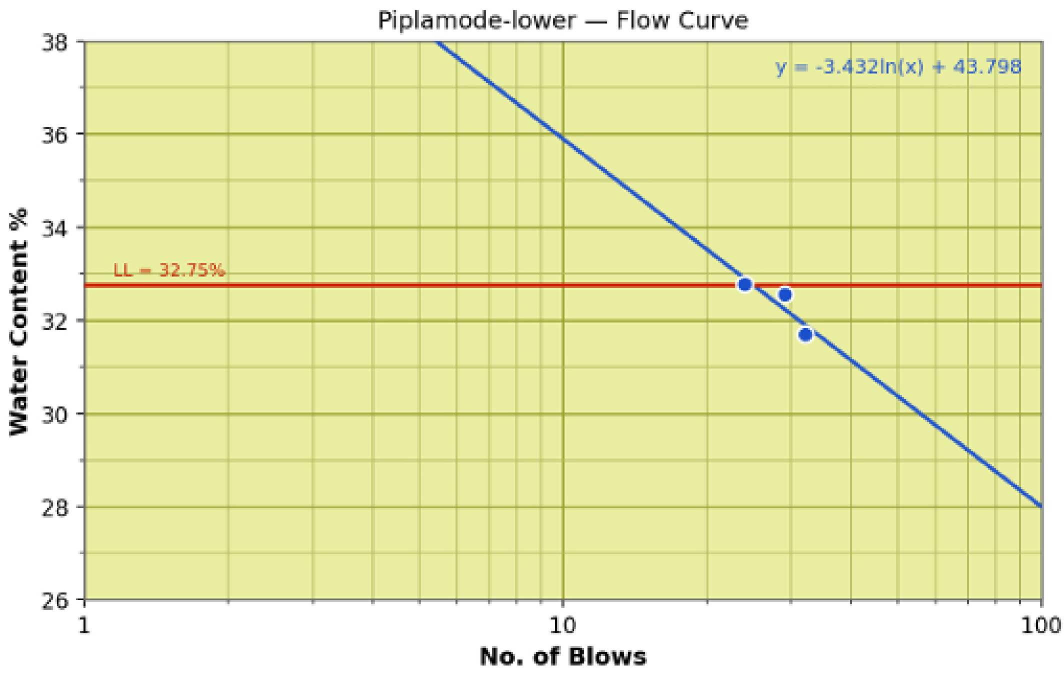

A.2 Plastic Limit and Plasticity Index

S.No.	Observation	Det. 1	Det. 2	Det. 3
1	Mass of empty can (M1) (gm)	18.00	17.84	17.26
2	Mass of can + wet soil (M2) (gm)	20.46	19.63	18.91
3	Mass of can + dry soil (M3) (gm)	19.95	19.27	18.59
4	Mass of water = M2 − M3 (gm)	0.51	0.36	0.32
5	Mass of dry soil = M3 − M1 (gm)	1.95	1.43	1.33
6	Water Content (%)	26.154	25.175	24.060
	Plastic Limit (PL)	**25.130**		
	Plasticity Index (PI = LL − PL)	**7.623**		

A.3 Specific Gravity

S.N	Description	Sample 1	Sample 2
1	Pycnometer No.	S2N1	S2N2
2	Mass of Empty Pycnometer (M1) gm	564.00	582.00
3	Mass of Pycnometer + Soil (M2) gm	680.00	720.00
4	Mass of Pycnometer + Soil + Water (M3) gm	1636.00	1656.00
5	Mass of Pycnometer + Water (M4) gm	1562.00	1570.00
6	Specific Gravity (G)	2.76	2.65
	Average Specific Gravity	**2.71**	

A.4 California Bearing Ratio (CBR) Test

CBR Test: The Pipalamod Lower subgrade CBR of 5.86% exceeds the DoR threshold of CBR > 5% specified as a site selection criterion by the supervisor. This means the subgrade is classified as medium strength (IRC 37 CBR range 5-7%) and the standard IITPave design equations apply without the need for special subgrade treatment. Sites with CBR < 5% (Pipalamod Upper, Richoktar, Bishaltar, Galchhi height) were excluded from this study on this basis.

Penetration (mm)	Load Dial Reading	Unit Load (kg/cm^2)
0.0	0	0.0000
0.5	4	0.2037
1.0	11	0.5475
1.5	20	1.0313
2.0	32	1.6552
2.5	46	2.3173
4.0	90	4.5837
5.0	121	6.1497
7.5	163	8.3015
10.0	202	10.2878
12.5	246	12.5541

Corrected Unit Load at 2.5 mm	2.3173 kg/cm^2
Corrected Unit Load at 5.0 mm	6.1497 kg/cm^2
Corrected CBR at 2.5 mm	**3.31%**
Corrected CBR at 5.0 mm	**5.86%**

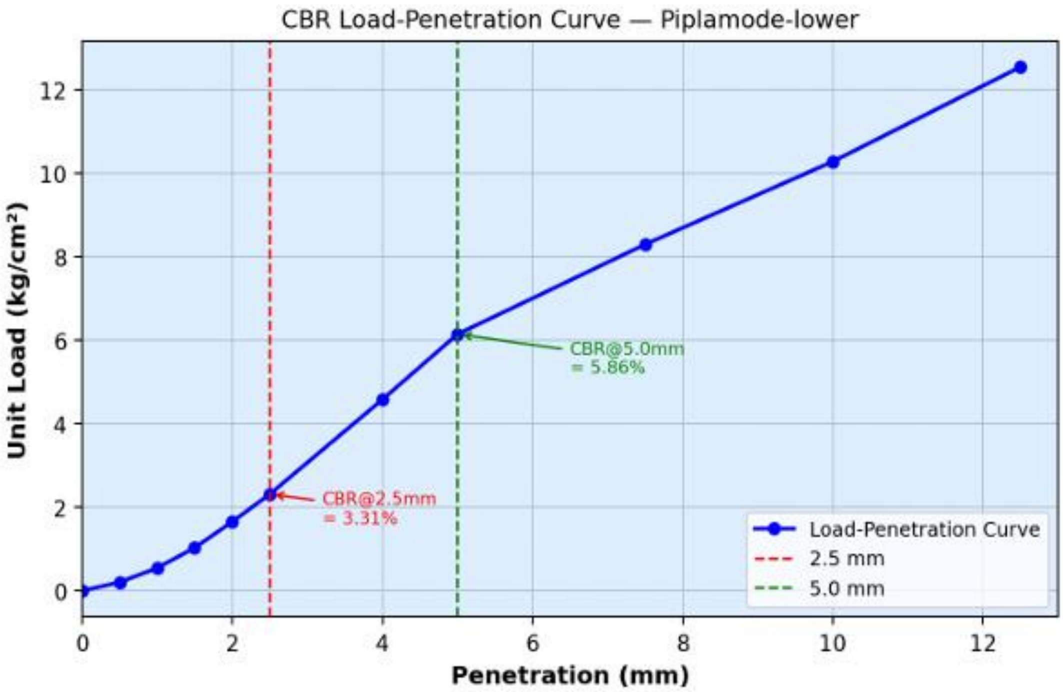

The optimum moisture content (OMC) is 10% with max dry density 1.56gm/cc.

A.5 Direct Shear Test

Specimen Properties	
Wt. of Wet Soil (gms)	54.64
Volume of Soil (cc)	46.82
Wet Density (g wet)	1.17

Normal Stress (kg/cm^2)	Peak Shear Stress (kg/cm^2)
0.1538	0.2683
0.3076	0.3772
0.4614	0.4563

Angle of Internal Friction (ϕ)	**31.43°**
Cohesion (c)	**0.1793 kg/cm^2**

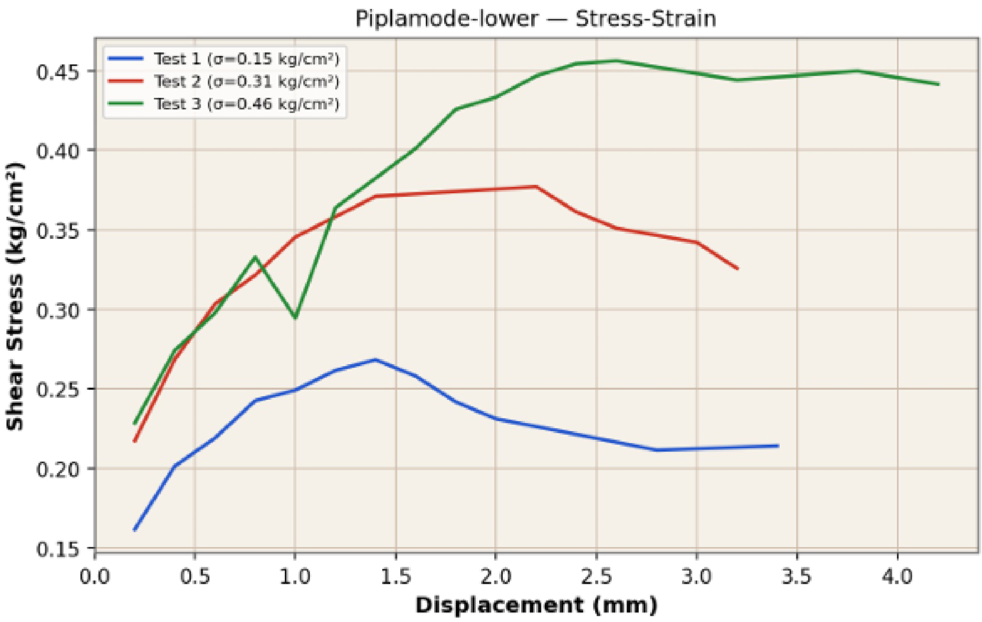

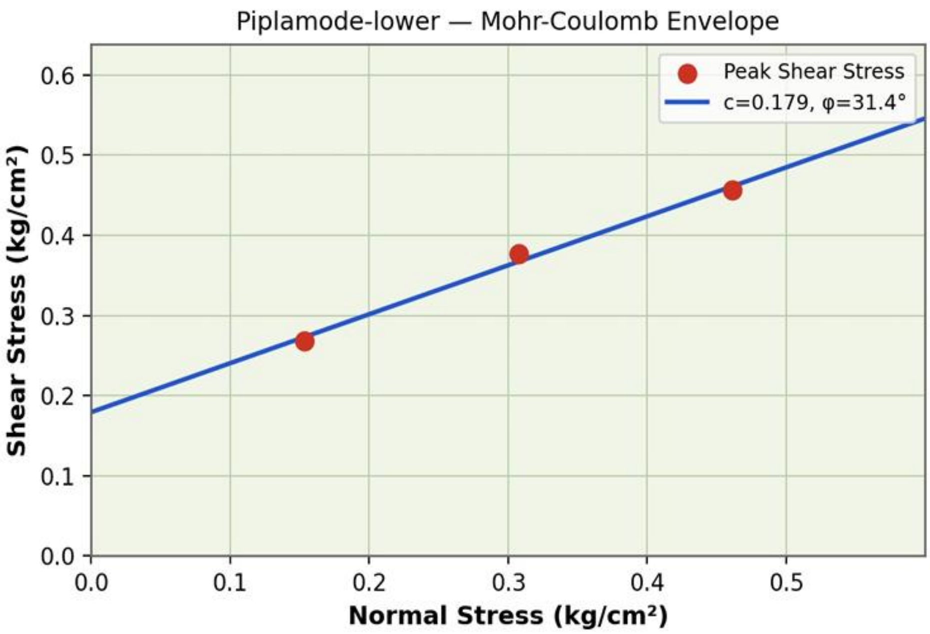

A.6 Grain Size Distribution Test

Sieve Size (mm)	Retained (gm)	Cum. Retained (gm)	Passing (%)
38.1	—	0.00	100.00
25.4	—	0.00	100.00
19.1	—	0.00	100.00
12.7	—	0.00	100.00
10.0	—	0.00	100.00
4.75	50.00	50.00	90.00
2.36	12.00	62.00	87.60
1.18	10.00	72.00	85.60
0.6	4.00	76.00	84.80
0.3	2.00	78.00	84.40
0.15	6.00	84.00	83.20
0.075	20.00	104.00	79.20

Total Sample Weight (gm)	500.00
Specific Gravity (Gs)	2.72
Passing 0.075 mm (%)	**79.20**

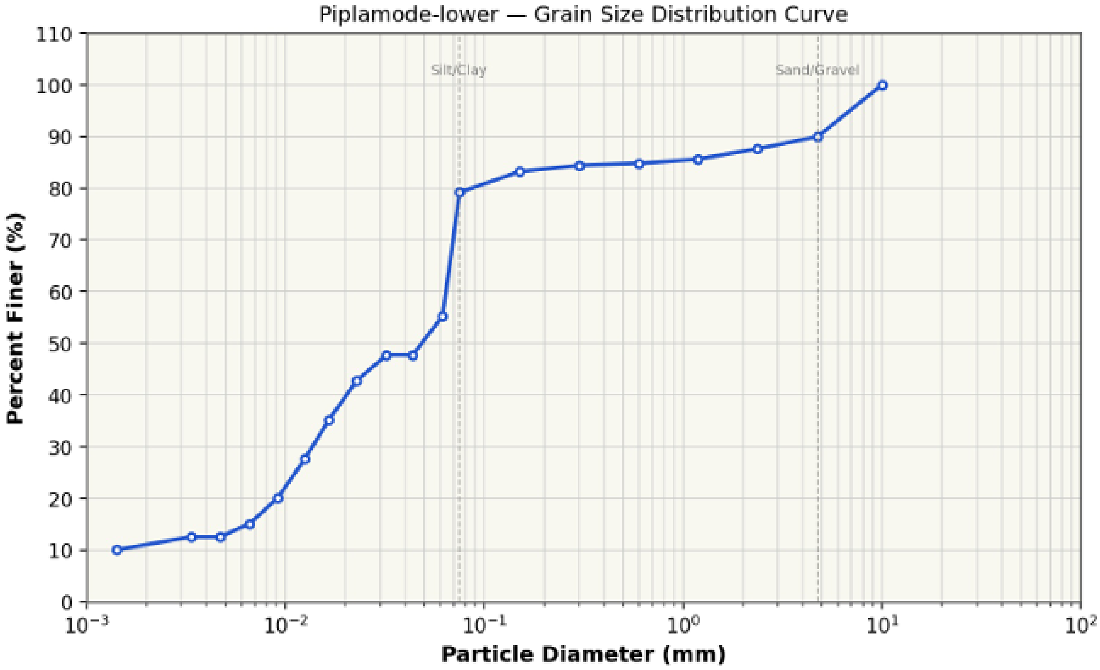

A.7 Consolidation Test

Parameter	Value
Specific Gravity, G_s (IS 2720 Part 3)	2.71
OMC / Initial Water Content, w (%) (IS 2720 Part 7)	10.0
Maximum Dry Density, γ_d (g/cc) (IS 2720 Part 7)	1.56
Initial Void Ratio, $e_0 = G_s \gamma_w / \gamma_d - 1$ (IS 2720 Part 15, Cl. 5)	0.7372
Degree of Saturation at Compaction, S_r (%)	36.8
Initial Sample Height, H_0 (mm)	18.4
Height of Solids, $H_s = H_0/(1+e_0)$ (mm)	10.5919
Ring Diameter (cm)	6.0
Compression Index, C_c (IS 2720 Part 15, Cl. 7)	**0.0443**
R^2 of NCL regression	0.9876
NCL pressure range used (t/m^2)	0.866–111.752

: e–$\log_{10} p$ Data — Piplamode Lower (shaded rows used for NCL regression, IS 2720 Part 15: 1986)

No.	Pressure (t/m^2)	Dial (1440 min)	ΔH (mm)	$2H$ (mm)	Void Ht. $(2H - H_s)$ (mm)	Void Ratio e
1	0.4330	1500	0.000	18.4000	7.8081	0.73718
2	0.8660	1492	0.016	18.3840	7.7921	0.73567
3	2.6670	1375	0.250	18.1500	7.5581	0.71358
4	7.1870	1243	0.514	17.8860	7.2941	0.68865
5	16.1890	1204	0.592	17.8080	7.2161	0.68129
6	28.8640	1157	0.686	17.7140	7.1221	0.67241
7	60.7910	1066	0.868	17.5320	6.9401	0.65523
8	111.7520	972	1.056	17.3440	6.7521	0.63748

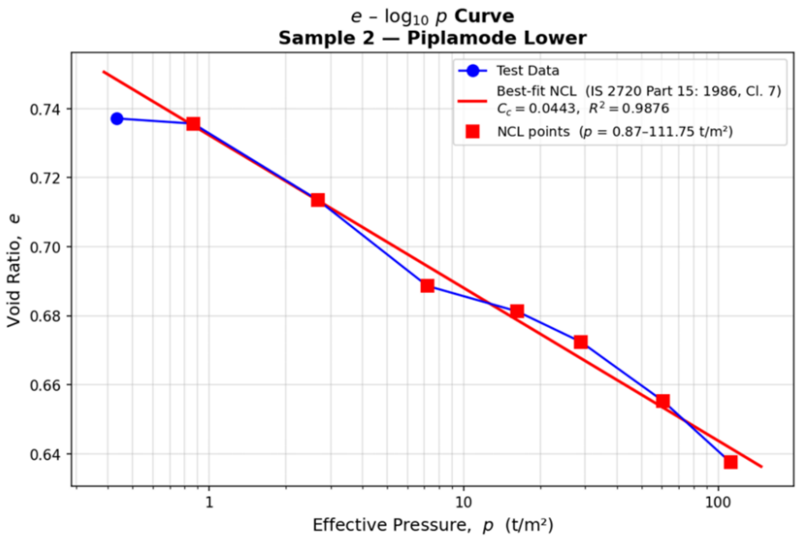

Figure 42: e–$\log_{10} p$ *Curve — Piplamode Lower (IS 2720 Part 15: 1986, Cl. 7). Best-fit NCL line (red) over* $p = 0.866$–$111.752\ t/m^2$; $C_c = 0.0443$, $R^2 = 0.9876$.

APPENDIX B: PAVEMENT DESIGN CALCULATIONS USING IITPAVE

The IITPave software implements the IRC 37 (2018) mechanistic-empirical pavement design framework. The following presents the design calculation procedure and output for Pipalamod Lower, redesigned for a cumulative design traffic of 145 MSAL confirmed by the Department of Roads.

B.1 Design Parameters

Table B.1: IIT Pave design inputs: pipalamod lower (145 MSAL)

Parameter	Value	Source
Cumulative design traffic	145 MSAL	Department of Roads, Nepal (2024)
Subgrade CBR	5.86%	Laboratory testing (IS 2720 Part 16)
Subgrade Resilient Modulus (Mr)	54.57 MPa	(IRC 37, CBR > 5%)
Asphalt type	Dense Bituminous Macadam (DBM)	Standard specification for Nepal highway
Asphalt modulus (Asphalt)	3000 MPa	IRC 37 standard at 35°C for this traffic range
Granular base modulus (Base)	165.37 MPa	IITPave output for CBR = 5.86%
Reliability level	90%	IRC 37 standard for National Highways
Design parameter fatigue	ε_t at BoA ≤ ε_t (allowable)	IRC 37 Equation 3.4
Design parameter rutting	ε_{zz} at ToS ≤ ε_v (allowable)	IRC 37 Equation 3.2

B.2 Design Output: Pavement Layer Thicknesses

Site: Pipalamod Lower

B.2.1. Given data

CBR of Subgrade = 5.86%

B.2.2. Resilient modulus of subgrade (MR)

For CBR ≥ 5%, the formula is:

$$M_r = 17.6 \times (CBR)^{0.64}\ (MPa)$$

Substituting CBR = 5.86%:

$$M_r = 17.6 \times (5.86)^{0.64}$$

$$= 54.57\ MPa$$

B.2.3. Base layer thickness

For granular base, the resilient modulus formula is:

$$M_{r(base,granular)} = 0.2 \times h^{0.45} \times M_{r(support)}$$

Let h = 420 mm:

$$M_{r(base)} = 0.2 \times (420)0.45 \times 54.57$$

$$= 165.37\ MPa$$

B.2.4. Adopted layer thicknesses

Asphalt Layer (DBM): 200 mm → 3000 MPa

Base Layer (WMM): 420 mm → 165.37 MPa

B.2.5. Design traffic

MSAL for design period of 15 years = 145 MSAL (DoR)

B.2.6. Rutting criteria

For rutting, the allowable vertical compressive strain (ε_v):

$$145 \times 10^6 = 1.4100 \times 10^{-8} \times \left(\frac{1}{\varepsilon v}\right)^{4.5337}$$

$$\therefore\ \varepsilon_{v(rut)} = 0.000294\ (Allowable)$$

B.2.7. Fatigue criteria

For fatigue, taking E_1 = 3000 MPa for the bituminous layer:

$$145 \times 10^6 = 0.5161 \times C \times 10^{-9} \times \left(\frac{1}{\varepsilon_t}\right)^{3.89} \times \left(\frac{1}{M_{rm}}\right)^{0.89}$$

$$\therefore \varepsilon_{t(fatigue)} = 0.0001461\ (Allowable)$$

B.2.8. Verification (IIT-Pave Software)

Checking rutting and fatigue criteria using IIT-Pave Software:

$$\varepsilon_{v(rut)} = 0.000288\ (< 0.000294\ Allowable)$$

$$\varepsilon_{t(fatigue)} = 0.000145\ (< 0.0001461\ Allowable)$$

Design is satisfactory for both the rutting and the fatigue criteria.

Table B.2: IITPave pavement layer design output

Layer	Thickness (mm)	Modulus (MPa)	Poisson's Ratio	Material
Bituminous Asphalt (DBM)	200	3000	0.35	Dense Bituminous Macadam
Granular Base Course	420	165.37	0.35	WBM/Crushed Stone Base
Subgrade (natural)	5000	54.57 (M_r)	0.35	Silty clay

APPENDIX C: LAB TEST PHOTOS

Fig: Vehicle survey

General	
Model	PLAXIS 3D
Elements	10-Noded
Acceleration	
Gravity	1.0 G (-Z direction)
Earth gravity	9.810 m/s²
Mesh	
Nr of soil elements	23935
Nr of nodes	54926
Average element size	0.7118 m
Maximum element size	4.287 m
Minimum element size	2.814E-3 m
Comments	

Fig: General information of model

APPENDIX D: SCRIPTS USED IN PYTHON EDITOR

D.1 Scripts to Create Whole Point Loads Setup

```
import math
from plxscripting.easy import *
# --- 1. CONNECTION ---
PORT =
PASSWORD = ''
try:
    s_i, g_i = new_server('', PORT, password='')
    print("Connected to PLAXIS 3D")
except Exception as e:
    print(f"FAILED TO CONNECT: {e}")
    exit()
# --- 2. UPDATED PARAMETERS ---
num_points =
arc_angle_deg =
radius =
start_y =
base_z =
slope =
# Convert degrees to radians for the loop limit
arc_angle_rad = (arc_angle_deg * math.pi) / 180
alpha = math.atan(slope)
# --- 3. GENERATION LOOP ---
print(f"Creating {num_points} loads over a {arc_angle_deg} degree arc...")
```

```
    # Calculate coordinates
    x_final = radius * math.sin(t)
    y_rel = radius * (1 - math.cos(t))
    y_final = start_y + (y_rel * math.cos(alpha))
    z_final = base_z + (y_rel * math.sin(alpha))
      # Create the load
    res = g_i.pointload(x_final, y_final, z_final)
      if res:
      target_load =
      target_load.Fz =
      target_load.Name = f"Point_{i+1}"
    else:
      print(f"Warning: Load {i} at ({x_final:.2f}, {y_final:.2f}) was merged.")
# --- 4. FINALIZE ---
try:
    g_i.save()
    print(f"SUCCESS: {num_points} point loads created.")
except:
    print("Loads created, but could not auto-save.")
```

D.2 Scripts to Create Phases

```
from plxscripting.easy import *
# 1. Setup Connection
localhost_port =
password = ''
try:
    s, g_i = new_server('localhost', localhost_port,
password='%XDyE9r<3g$B$g/~')
    g_i.gotostagedconstruction()
```

```
    print("Connected successfully.")
except:
    print("Connected. Please ensure you are on the 'Staged Construction' tab.")
print("Starting phase creation and configuration...")
for i in range(1, 101):
    # --- STEP 1: CREATE THE PHASE ---
    new_phase = g_i.phase(parent_phase)
    phase_name = f"Phase_{i}"

    # --- STEP 2: HANDLE SOIL ACTIVATION ---
    # Activate the 3 soil volumes in this phase
    for soil in soils_to_activate:

    # --- STEP 3: HANDLE POINT LOADS ---
    load_a_name = f"PointLoad_{i}"
    load_b_name = f"PointLoad_{i + 3}"
    # Deactivate all point loads first to ensure a clean slate
    g_i.deactivate(g_i.PointLoads, new_phase)
        # Activate the specific two loads
    if hasattr(g_i, load_a_name):
            if hasattr(g_i, load_b_name):
        g_i.activate(getattr(g_i, load_b_name), new_phase)
    # Chain the phases (Phase 2 starts from Phase 1)
        print(f"Configured {phase_name}: Soils active + {load_a_name} &
{load_b_name}")
print("\nAll 100 phases updated! Starting calculation...")


print("Calculation started. Check the PLAXIS window for progress.")
```

D.3 Scripts to Update Load

```
import pandas as pd
from plxscripting.easy import *
# 1. Configuration: Match your PLAXIS Remote Scripting settings
PORT = 10000
PASSWORD = ''
FILE_PATH =
# Connect to the active PLAXIS 3D session
s_i, g_i = new_server('localhost', PORT, password='%XDyE9r<3g$B$g/~')
current_phase_obj = None
fz_fixed = -35
            # Process Point ID rows (e.g., "Point_7")
    if cell_raw.startswith("Point_") and current_phase_obj:
        try:
            # Transform ID: Point_7 -> PointLoad_7_1
            id_num = cell_raw.split('_')[-1]
            pl_name = f"PointLoad_{id_num}_1"
                    # Find the PointLoad object in the PLAXIS model
            pl_obj = getattr(g_i, pl_name)
            # Extract Fx and Fy values (Last two columns in your sheet)
            fx_val = float(row.iloc[-2])
            fy_val = float(row.iloc[-1])
            # DIRECT ASSIGNMENT to the PLAXIS model for the current phase
            pl_Fx[current_phase_obj] = fx_val
            pl_ Fy[current_phase_obj] = fy_val
            pl_o.Fz[current_phase_obj] = fz_fixed
                    # Optional: Ensure the load is activated in this phase
            pl_obj.Active[current_phase_obj] = True
```

```
        except Exception as e:
            print(f"Failed to update {cell_raw} at row {index}: {e}")
print("Update Complete.")
```

D.4 Scripts to Extract output

```
import os
import pandas as pd
from plxscripting.easy import *
# 1. Connection & Model List
PORT = 10000
PASSWORD = '%XDyE9r<3g$B$g/~'
#phase_mapping = {
  }
all_results = []
# 3. Extraction Automation
try:
  s_o, g_o = new_server('localhost', PORT, password=PASSWORD)
    for path in model_paths:
    m_name = os.path.basename(path).replace(".p3dat", "")
    print(f"Opening: {m_name}")

    for ph_idx, coords in phase_mapping.items():
      try:
        phase = g_o.Phases[ph_idx]
                    all_results.append(row)
                print(f"Phase {ph_idx} skip: {e}")

  # 4. Sorting & Multi-Sheet Comparison
  df = pd.DataFrame(all_results)
```

```
   output = "Complete_GH_output_300_check.xlsx"
     with pd.ExcelWriter(output) as writer:
     df.to_excel(writer, sheet_name="MasterData", index=False)
         # Results list for comparison sheets
     result_types = [ "E3"]
         for res_name in result_types:
       # Create a comparison table for each layer (BoA, MoB, ToS)
       for layer in ["BoA", "MoB", "ToS"]:
         pivot_name = f"{layer}_{res_name}"
           print(f"\nSUCCESS! Multi-model comparison report generated: {output}")
except Exception as e:
   print(f"Global Error: {e}")
```

Only the snippets of the scripts are attached in Appendix D. Python scripting was used for other steps of works too. Only some are presented in appendix.

APPENDIX E: LIST OF PUBLICATIONS

Conference Paper:

P. Shrestha and R.C. Tiwari, "3D FEM-Based Analysis of Geogrid-Reinforced Flexible Pavement on Curved-Gradient Alignment Subjected to Heavy Axle Loads" in *18^{th} IOE GRADUATE CONFERENCE (2026)*, Lalitpur, Nepal.